Regime-oriented causal model evaluation of Atlantic-Pacific teleconnections in CMIP6

Soufiane Karmouche[1,2], Evgenia Galytska[1,2], Jakob Runge[3,4], Gerald A. Meehl[5], Adam S. Phillips[5], Katja Weigel[1,2], and Veronika Eyring[2,1]

[1]University of Bremen, Institute of Environmental Physics (IUP), Bremen, Germany
[2]Deutsches Zentrum für Luft- und Raumfahrt (DLR), Institut für Physik der Atmosphäre, Oberpfaffenhofen, Germany
[3]Deutsches Zentrum für Luft- und Raumfahrt (DLR), Institut für Datenwissenschaften, Jena, Germany
[4]Technische Universität Berlin, Berlin, Germany
[5]National Center for Atmospheric Research (NCAR), Boulder, CO, USA

Correspondence: Soufiane Karmouche (sou_kar@uni-bremen.de)

Abstract.

The climate system and its spatio-temporal changes are strongly affected by modes of long-term internal variability, like the Pacific Decadal Varibility (PDV) and the Atlantic Multidecadal Variability (AMV). As they alternate between warm and cold phases, the interplay between PDV and AMV varies over decadal to multidecadal timescales. Here, we use a causal discovery method to derive fingerprints in the Atlantic-Pacific interactions and investigate their phase-dependent changes. Dependent on the phases of PDV and AMV, different regimes with characteristic causal fingerprints are identified in reanalyses in a first step. In a second step, a regime-oriented causal model evaluation is performed to evaluate the ability of models participating in the Coupled Model Intercomparison Project Phase 6 (CMIP6) in representing the observed changing interactions between PDV, AMV and their extra-tropical teleconnections. The causal graphs obtained from reanalyses detect a direct opposite-sign response from AMV on PDV when analysing the complete 1900-2014 period, and during several defined regimes within that period, for example, when AMV is going through its negative (cold) phase. Reanalyses also demonstrate a same-sign response from PDV on AMV during the cold phase of PDV. Historical CMIP6 simulations exhibit varying skill in simulating the observed causal patterns. Generally, Large Ensemble (LE) simulations showed better network similarity when PDV and AMV are out of phase compared to other regimes. Also, the two largest ensembles (in terms of number of members) were found to contain realizations with similar causal fingerprints to observations. For most regimes, these same models showed higher network similarity when compared to each other. This work shows how causal discovery on LEs complements the available diagnostics and statistics metrics of climate variability to provide a powerful tool for climate model evaluation.

1 Introduction

Modes of natural climate variability from interannual to multidecadal timescales have large effects on regional and global climate with important socio-economic impacts. Despite their importance, systematic evaluation of climate models and their simulation of internal variability remains a challenging task (Eyring et al., 2019). The available observational datasets are not

only short in time, but also hold considerable uncertainties that arise from errors in the data record during the pre-satellite era (Phillips et al., 2014; Fasullo et al., 2020; Eyring et al., 2021). Generally, in order to test their performance, the models are often compared to reanalysis datasets based on observations. This approach is a key to estimate the ability of models to correctly simulate internal variability. An evaluation study by Fasullo et al. (2020) showed a systematic improvement in the representation of modes of climate variability through the different phases of the Coupled Model Intercomparison Project (CMIP), where models largely capture the statistical properties of these modes (e.g., timescale, autocorrelation, spectral characteristics, and spatial patterns). However, across the CMIP archive, comparisons with observations also reveal remarking systematic errors. These are errors that have only little or no improvement due to the complexity of the climate system and the difficulty to assign a specific cause to a specific systematic error or bias (Stouffer et al., 2017; Fasullo et al., 2020; Eyring et al., 2021).

It is therefore a priority to go beyond spatial and spectral properties and apply new approaches that reveal whether a climate model correctly simulates the observed lagged teleconnections between remote regions. Here, causal discovery methods provide a way to estimate such dynamical climate dependencies from data timeseries (Ebert-Uphoff and Deng, 2012; Runge et al., 2019b; Runge, 2020; Runge et al., 2019a; Nowack et al., 2020). Causal graphs not only help to assess the degree to which a climate model recreates well-defined connections within the climate system, but also to determine if specific phenomena are simulated for the right reasons. As the nature of these connections and phenomena is supposed to vary depending on the state of multidecadal processes of internal climate variability, we investigate the causal relations not only for the complete historical period, but also for shorter, state-dependent timescales that define different regimes of dependencies.

In this study, we utilize a regime-oriented causal analysis on indices of dominant modes of long-term variability over the Atlantic and Pacific to investigate the interactions between the two basins in CMIP Phase 6 historical simulations (CMIP6, Eyring et al., 2016) as well as in Large Ensembles (LE) and compare those results to reanalysis data. To do so, we first calculate the two leading modes of multidecadal coupled (ocean-atmosphere) climate variability over the Pacific and Atlantic: Pacific Decadal Variability (PDV) and Atlantic Multidecadal Variability (AMV). PDV, encompassing a symmetric variability pattern over the North and South Pacific (Mantua et al., 1997; Chen and Wallace, 2015), with an El Niño-Southern Oscillation-(ENSO) like decadal variability over the tropical Pacific extending over the entire Pacific basin (Nitta and Yamada, 1989; Zhang et al., 1997; Meehl et al., 2013), can be defined by Pacific sea surface temperature (SST) anomaly fields. Its influence on the other hand, expands well beyond the Pacific affecting regional- and global-scale climate on decadal timescales. Its temporal evolution is characterized by an interannual and decadal variability with some pronounced shifts, notably the extensively studied 1976/77 transition (Zhang et al., 1997; Power et al., 1999; Mantua et al., 1997; Arblaster et al., 2002; Meehl et al., 2009). In particular, Ebbesmeyer et al. (1991) identified dramatic changes in the North Pacific biota and climatic variables during that period. The positive PDV phase dominated during the period from the mid-1970s through late 1990s, while the following period of global warming hiatus entailed a switch to negative phase (Meehl et al., 2016; Fyfe et al., 2016). The second dominant pattern of internal multidecadal variability, the AMV, acts on the North Atlantic region. Sometimes referred to as the Atlantic Multidecadal Oscillation (AMO, Kerr 2000), AMV is characterized by a dipole SST variability pattern featuring opposite sign anomalies between the Tropical North Atlantic and South Atlantic (IPCC, 2021). Index timeseries of the observed AMV pattern show that the mode goes through preferred phases for multidecadal periods with the positive phase

persisting since the late 1990s to nowadays. The AMV was also discovered to have significant socio-economic and climate impacts, particularly on the Indian summer monsoon, North American and European summer climate and hurricanes over the Atlantic (Folland et al., 1986; Sutton and Hodson, 2005; Knight et al., 2006; Zhang and Delworth, 2006; Si and Hu, 2017; Yan et al., 2017).

Previous research focused on Atlantic-Pacific interactions suggests changing forcing mechanisms can be applied by one basin on the other (d'Orgeville and Peltier, 2007; Wu et al., 2011; Kucharski et al., 2016; Nigam et al., 2020). Observational analyses concluded that the multidecadal component of the negative PDV phase can lag the positive AMV phase by about a decade (Zhang and Delworth, 2007; d'Orgeville and Peltier, 2007). Literature suggests a PDV-AMV link through a tropical pathway where increasing Atlantic temperatures instigate a La Niña-like cooling in the equatorial Pacific, and a consequent weakened Aleutian low in the North (McGregor et al., 2014; Kucharski et al., 2016; Li et al., 2016; Ruprich-Robert et al., 2017). Meehl et al. (2021a) showed that the Atlantic and Pacific are mutually and sequentially interactive and are connected mainly through the atmospheric Walker circulation with some extra-tropical contributions. Components of the PDV in that study were found to be linked to Aleutian low variability associated with the Pacific-North American (PNA) pattern (Wallace and Gutzler, 1981), a prominent mode over the Northern Hemisphere extra-tropics, with a quadrupole anomaly field of 500 hPa geopotential height (H500) that can influence the subtropical North Atlantic. Teleconnections to the Southern Hemisphere were also noted by Meehl et al. (2021a) involving the Pacific-South-American (PSA) pattern that ends up influencing the subtropical South Atlantic. Another study involving coupled model simulations from Zhang et al. (2018) agreed with Meehl et al. (2021a) and showed that the PSA, which can be thought of as the South Pacific counterpart of PNA, generates a forcing that translates into the Southern Hemisphere component of PDV. To assess these possible extra-tropical connections, in addition to PDV and AMV, we include in our causal discovery study indices for both PNA and PSA modes. The indices of the latter modes are both based on sea level pressure (SLP) anomalies. PSA is generally expressed through two modes, in this study we use PSA mode 1 (PSA1) index as the second Empirical Orthogonal Function (EOF) of area-weighted SLP anomalies in the South Pacific (Mo and Higgins, 1998, see Methods).

Figure 1 shows the various steps of our regime-oriented causal model evaluation approach presented in this paper, which we organise as follows: Sect. 2 describes methods (Sect. 2.1) and data (Sect. 2.2) that were used in this study. In Sect. 2.1.1 we present the package used to generate the indices and spatial patterns of the different modes of climate variability. This is followed by an introduction to the causal discovery method (Sect. 2.1.2), and the framework for the regime-oriented causal model evaluation (Sect. 2.1.3). In Sect. 2.1.4 we introduce the causal network comparison method via calculation of F_1-scores. The analysed reanalysis datasets and CMIP6 models used in this study are listed in Sect. 2.2. The Results (Sect. 3) start with a correlation analysis to compare the SST and SLP regression maps associated with the CMIP6-simulated timeseries of AMV, PDV, PNA and PSA to those from reanalysis data (Sect. 3.1). As the causal analysis only uses timeseries information of the calculated indices, this comes as a sanity check to measure the similarity between the observed and simulated spatial patterns associated with the index timeseries. This is followed by Sect. 3.2 where we show the causal networks from reanalysis data during different regimes. These serve as reference for the regime-oriented causal model evaluation in the subsequent Sect. 3.3. We discuss the results in Sect. 3.4 before closing the paper with a summary in Sect. 4.

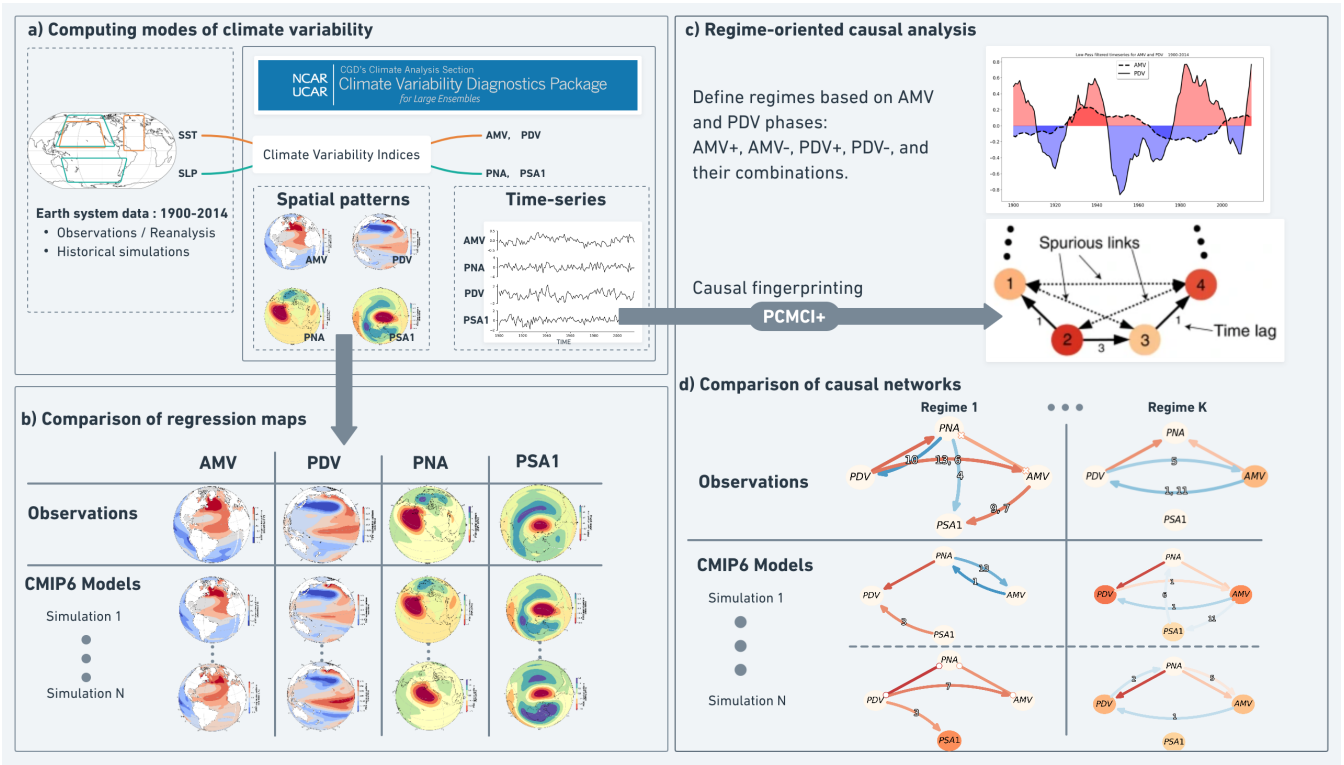

Figure 1. Framework for the regime-oriented causal model evaluation. a) Gridded SST and SLP data used to calculate indices for AMV, PDV, PNA and PSA1 modes of climate variability. Diagnostics from the NCAR Climate Variability Diagnostic Package for Large-Ensembles (CVDP-LE) produce the timeseries of these indices and their associated spatial patterns (regression maps). b) We first, as a sanity check, compare the CMIP6 model-simulated SST (for AMV and PDV) and SLP (for PNA, PSA1) regression maps to those from reanalysis before c) using the timeseries of the four indices for the regime-oriented causal analysis. Here we define different regimes depending on the sign of the 13-year low-pass filtered AMV and 11-year low-pass filtered PDV timeseries. For every regime we run PCMCI+ to estimate instantaneous and lagged links between nodes representing the timeseries of the indices calculated in (a) from the reanalyses and model data. In this schematic example, there are four indices, with node color indicating auto-correlation, and there is a causal link (solid black arrow) between index 2 and indices 1 and 3, and then there is a causal link between indices 3 and 4. The method identifies and removes spurious links (see black dashed arrows) between indices 1 and 4, or 2 and 4. Unitless representative time lags are labeled on each causal link, where index 1 lags index 2 by one time-step (depending on temporal resolution of the timeseries, here yearly), index 3 lags index 2 by three, and index 4 lags index 3 by one. Applying the method to the timeseries in (a) provides d) dataset- and regime-specific causal fingerprints in a similar format to the schematic in (c), which can be used for model evaluation and intercomparison. We calculate annual averages from the monthly timeseries of PDV and AMV provided by CVDP-LE. This way, the dataframe is fit for multi-year and decadal causal estimations. In addition to the subtraction of global mean temperatures in the CVDP-LE calculation of PDV and AMV, the causal networks are estimated after linearly detrending the timeseries of the four indices to ensure their stationarity. The estimated causal dependencies (links) are hence assumed to be a mixture of internal variability and time-varying anthropogenic forcing (mainly from aerosols).

2 Methods and Data

2.1 Methods

2.1.1 Climate Variability Diagnostic Package

Developed by the National Center for Atmospheric Research (NCAR), the Climate Variability Diagnostic Package for Large Ensembles (CVDP-LE) provides an analysis tool for the evaluation of the major modes of internal climate variability tailored for large-ensemble climate models (Phillips et al., 2020). It includes diagnostics to compute indices for the major modes of coupled and large-scale atmospheric climate variability. The package also offers comparison metrics for the spatial and temporal patterns with respect to reference observational datasets.

For the indices of our selected modes of climate variability (see enumeration below), we use the diagnostic results computed from the CMIP6 LE historical simulations and from reanalyses data over the 1900-2014 period. These are calculated by the CVDP-LE and publicly available as Network Common Data Format (NetCDF) files on the Community Earth System Model (CESM) Climate Variability and Change Working Group's (CVCWG) CVDP-LE Data Repository under https://www.cesm.ucar.edu/working_groups/CVC/cvdp-le/data-repository.html. We use index timeseries and their associated spatial patterns (SST regression maps for AMV and PDV, PSL regression maps for PNA and PSA1). The indices used in this analysis are computed by the CVDP-LE package as follows:

1. PDV Index (sometimes referred to as the PDO index): is defined as the standardized principal component (PC) timeseries associated with the leading EOF of area-weighted monthly SST anomalies over the North Pacific region [20-70N, 110E-100W] minus the global mean [70N-60S] (effectively detrending the data). (Mantua et al., 1997)

2. AMV Index (sometimes referred to as the AMO index): is defined as monthly SST anomalies averaged over the North Atlantic region [0-60N, 80W-0W] minus the global mean [60N-60S] (effectively detrending the data). (Trenberth and Shea, 2006)

3. Pacific-North American Pattern (PNA): the leading EOF of area-weighted sea level pressure (SLP) anomalies over the region [20-85N, 120E-120W]. We use timeseries constructed from yearly winter December-January-February (DJF) means.

4. Pacific–South American Pattern Mode 1 (PSA1) second EOF of area-weighted SLP anomalies south of 20S (Mo and Higgins, 1998). We use timeseries calculated from annual means (ANN).

The idea behind subtracting the global mean in the definition of the SST-based modes, PDV and AMV, is to reduce potential effects of external greenhouse gas (GHG) forcing. The space- and time-varying aerosol forcing, however, is expected to contribute to the Atlantic and Pacific SST variability represented by the calculated AMV and PDV indices (Booth et al., 2012; Smith et al., 2016; Watanabe and Tatebe, 2019; Meehl et al., 2021a). According to their CVDP-LE definitions above, the calculations of PNA and PSA1 do not include any detrending. This is because, in models, the externally-forced component

of these SLP-based modes (unlike the SST-based ones) can generally be neglected when compared to the internally-generated component (Deser et al., 2012; Phillips et al., 2020). Thus, we presume that the aforementioned indices calculated by CVDP-LE, although not exhibiting a trend, are a combination of internal variability and external aerosol forcing. This is true for model-simulated indices and the ones calculated from reanalysis data (with the exception of the observed PSA1 timeseries which include a noticeable trend, not shown). To compare the simulated spatial patterns to the observed ones (Sect. 3.1), we correlate the regression maps associated with the timeseries of the indices as they are calculated by the CVDP-LE (see enumeration above). Only prior to applying the causal discovery algorithm (Sect. 2.1.2) do we further remove any linear trend that might still be present in the data to ensure stationarity. Moreover, as the focus of the paper revolves around causal pathways on decadal (multi-year) timescales, we perform annual averages of the AMV and PDV timeseries as they are computed based on monthly means by the CVDP-LE. Hence, for all results to be presented in this paper, we maintain the presumption that the calculated climate variability indices (eventually their spatial patterns and causal fingerprints) represent a mixed response of internally-generated variability and external aerosol forcing.

2.1.2 PCMCI+ Algorithm

For the regime-oriented causal analysis, we use a Python package called Tigramite, freely available at https://github.com/jakobrunge/tigramite, designed to efficiently estimate causal graphs from timeseries datasets. The causal discovery framework within Tigramite is called PCMCI (Peter Clark Momentary Conditional Independence) (Runge et al., 2019b). Its suitability for the challenges of timeseries data as studied here, mainly high dimensionality due to the number of variables and time lags, as well as autocorrelation, was studied in Runge et al. (2019b); Runge (2020). While the PCMCI framework is also suitable for nonlinear dependencies, in this paper we focus on linear relationships and use an extended version of PCMCI called PCMCI+ that can not only detect lagged (time lag $\tau > 0$), but also contemporaneous ($\tau = 0$) causal links (Runge, 2020).

PCMCI+ consists of two principal phases: a skeleton discovery phase and an orientation phase. Considering a time-dependent system (X_t) of N variables $\mathbf{X_t} = (X_t^1, ..., X_t^N)$, the skeleton discovery starts first by applying the PC1 Markov set discovery algorithm which is based on the PC algorithm (named after its inventors, Peter Spirtes and Clark Glymour) on a completely connected graph. The iterative PC1 algorithm tests for every lagged pair of nodes (variables) $(X_{t-\tau}^i, X_t^j)$ whether they are conditionally independent on efficiently selected conditions of other lagged variables, and, if so, removes the adjacency between them. The lagged conditions at this stage serve to estimate for each variable X_t^j a superset of lagged parents $\widehat{\mathcal{B}}_t^-(X_t^j)$ for which the adjacencies are oriented by time-order. In this step there still can be spurious links due to contemporaneous confounders. Hence, in the second skeleton discovery step contemporaneous conditions are iterated over in momentary conditional independence (MCI) tests implemented with partial correlation:

$$\mathbf{X}_{t-\tau}^i \perp\!\!\!\perp X_t^j | \mathcal{S}, \widehat{\mathcal{B}}_t^-(X_t^j) \setminus \left\{X_{t-\tau}^i\right\}, \widehat{\mathcal{B}}_{t-\tau}^-(X_{t-\tau}^i)$$

where $\widehat{\mathcal{B}}_t^-(X_t^j)$ are the lagged conditions of X_t^j and $\widehat{\mathcal{B}}_{t-\tau}^-(X_{t-\tau}^i)$ are the (time-shifted) lagged conditions of $X_{t-\tau}^i$ obtained in the first step. By iterating through subsets $\mathcal{S} \subset \mathbf{X_t}$ of contemporaneous adjacencies, the algorithm fully removes spurious links. The partial correlation tests assume a t-statistic with degrees of freedom given by the effective sample size $n - 2 -$

$|\mathcal{S}, \widehat{\mathcal{B}}^-_t(X^j_t) \setminus \{X^i_{t-\tau}\}, \widehat{\mathcal{B}}^-_{t-\tau}(X^i_{t-\tau})|$. The result is a graph with lagged and contemporaneous adjacencies. Lagged adjacencies are oriented by time-order since causation can only go forward in time. This skeleton phase is followed by a collider orientation phase, which further orients contemporaneous links based on unshielded triples $X^i_{t-\tau} - X^k_t - X^j_t$ where $\tau \geq 0$. If X^k_t is not part of the separating set $\mathcal{S}$ that makes $X^i_{t-\tau}$ and X^j_t independent, then the triple is oriented as $X^i_{t-\tau} \to X^k_t \leftarrow X^j_t$. Further contemporaneous links are then oriented such that the graph does not include cycles (see rules R1-R3 in Runge, 2020). The resulting graph then contains directed lagged and contemporanous links, but also unoriented adjacencies indicating that the collider and orientation rules could not be applied (Markov equivalence), or a conflicting adjacency where different rules are conflicting, for example, due to finite sample issues. For visualization purposes the estimated timeseries graph is then aggregated in a process graph (Figure 2) that summarizes the causal dependencies and their time lags. The link strength can be estimated in different ways, for example as standardized (causal) regression coefficients (Runge et al., 2015; Runge, 2021), but here we use the MCI partial correlation values corresponding to the conditional independence test statistic above.

A full method description of the original PCMCI and its PCMCI+ extension along with their respective pseudo code, proofs of their asymptotic consistency, and numerical experiments can be found in Runge et al. (2019b) and Runge (2020), respectively. These works also explain the underlying assumptions under which the detected links can be interpreted causally. Most importantly, since unobserved confounders can still render links as spurious, the graphs are causal only with respect to the analysed variables. Applying more advanced methods (Gerhardus and Runge, 2020) that can deal with hidden variables would considerably deteriorate the reliability of causal graph inferences for the short sample sizes available here.

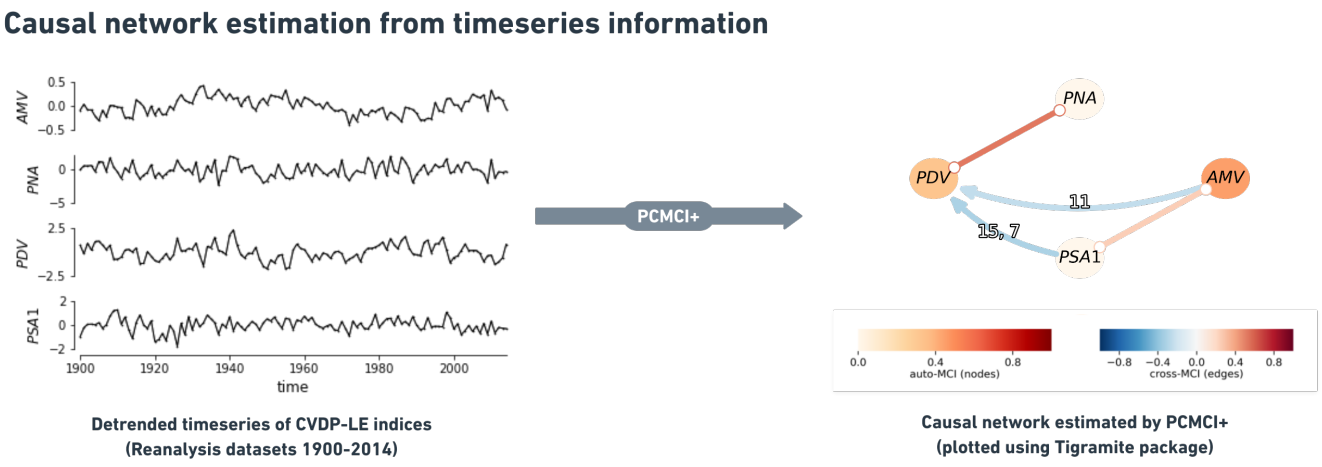

Figure 2. Constructing causal network using Tigramite by applying PCMCI+ on timeseries calculated by CVDP-LE from reanalysis datasets. Each node on a causal network (right) represents a variable (timeseries, left) and the node color its auto-correlation (self links of each variable). The link color shows the cross-MCI partial correlation value which denotes the sign and strength of the estimated causal link between two variables. The time lag for lagged links (curved arrows) are shown as small labels on the links. Straight lines represent instantaneous causal links happening with no time lag.

Figure 2 demonstrates the application of PCMCI+ algorithm on CVDP-LE datasets. Since causal discovery requires stationary timeseries (Runge, 2018), first we consider into our analysis detrended yearly 1900-2014 timeseries of modes of climate variability, namely AMV, PNA, PDV, and PSA1 (left). The resulting causal network from the application of PCMCI+ algorithm is shown in right (Figure 2). The direction, sign, strength (|cross-MCI| value) and time lag (τ) of the estimated causal links are all attributes that can be conveniently read off the generated causal graphs. Each node on a causal network represents a variable and the node color its auto-correlation (self-links of each variable). The link color shows the cross-MCI value which denotes the sign and strength of the estimated causal link between two variables. The time lag for lagged links (curved arrows) are shown as small labels on the links. For those connections that occur at multiple lags, the color of the link shows the strongest link, but the label depicts all significant lags sorted by their strength. The contemporaneous links are shown as straight arrows ("$\rightarrow$"; when directionality is decided), straight lines with circle-shaped ends ("o—o"; when the adjacency indicates a Markov equivalence), or straight lines with cross-shaped ends ("x—x"; indicating conflicting orientation rules).

With regards to the parameter settings for the PCMCI+ algorithm, we set the maximum time lag (τ_{max}) to 15 years ($\tau_{max} = 15$ time-steps, as we are using one data point per year). The significance level of the MCI partial correlation tests above α_{pc} is set to 0.05.

2.1.3 Set up for regime-oriented analysis

The teleconnections between the Pacific and Atlantic ocean basins are suggested to follow different regimes depending on the decadal phases that the AMV and PDV go through (Meehl et al., 2021a). In order to clearly identify the time periods of each phase, we smooth the timeseries data by applying 11-year and 13-year low-pass filters on PDV and AMV, respectively. Figure 3a shows the observed detrended low-pass filtered AMV and PDV timeseries used to specify the different phases and regimes for the masking before applying the PCMCI+ algorithm (the labeled regimes on the timeseries are only three out of the 10 we run the analysis over). First, running the analysis on the complete time period is intended to reveal the consistent causal dependencies throughout the complete historical timeseries (see Figure 2). The resulting causal networks from the complete period do not, however, expose much information on the causal effects which are changing over shorter time periods depending on how the PDV and AMV are varying during those phases. In order to identify these phase-dependent causal dependencies, we perform the analysis on multiple shorter periods (regimes) by selecting the time-steps that represent either the positive (warm) or negative (cold) phases based on the low-pass filtered indices, with AMV+(-) for when the value of low-pass filtered AMV is positive (negative), and the same for PDV+(-). We further split these regimes into combinations of warm and cold PDV and AMV phases (PDV+/AMV+, PDV+/AMV-, PDV-/AMV+, PDV-/AMV-). Additionally, since some regimes are too short to reveal any dependencies, we also opted to run the analysis for an 'In-Phase' regime that sums the PDV+/AMV+ and PDV-/AMV- periods. The remaining time-steps would then consist of the 'Out-of-Phase' regime for the period where the two low-pass filtered indices have opposite signs (PDV+/AMV- and PDV-/AMV+). This means that in addition to running it on the complete period, we apply the PCMCI+ algorithm on 10 different shorter time periods (within the original 1900-2014 period) for each dataset (see Figure 3a for reanalysis data). Figure 3b shows how we use the regimes defined in Figure 3a to mask the timeseries before applying the PCMCI+ method. This is shown for PDV+ and PDV- regimes as example. For each case,

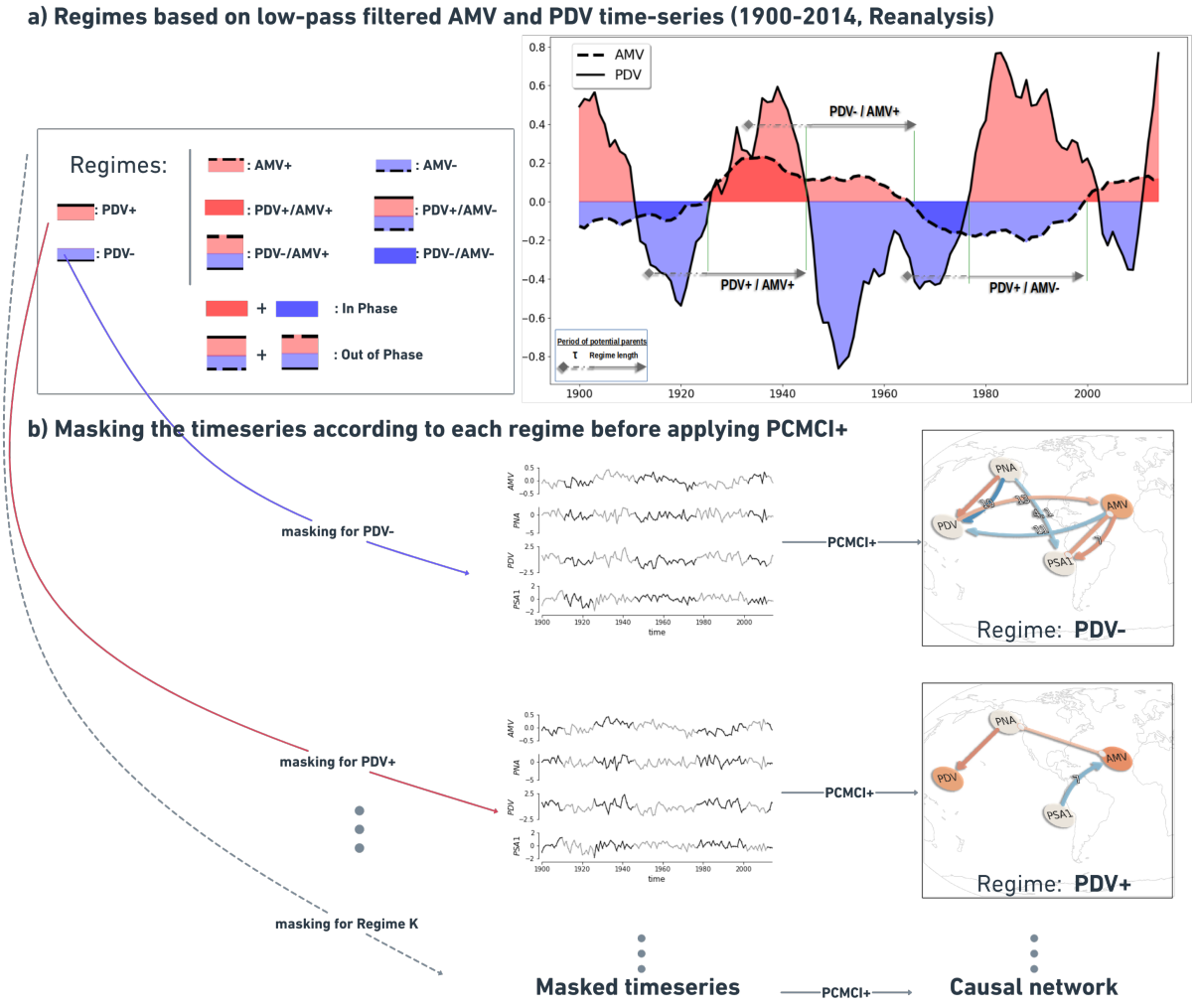

Figure 3. a) PDV and AMV timeseries calculated by CVDP-LE diagnostics on ERSSTv5 data are smoothed using 11 and 13-year low-pass filters, respectively. 10 regimes are defined (see table on the left) in addition to the 1900-2014 complete period. The PCMCI+ algorithm is applied on unfiltered (non-smoothed) PDV, AMV, PNA, PSA1 yearly detrended timeseries that are masked according to the periods that define each regime. The right arrows on the smoothed timeseries represent unmasked periods from three out of 10 regimes (PDV+/AMV+, PDV-/AMV+, and PDV+/AMV-). b) The regimes identified in (a) are used to mask the non-smoothed (but detrended) index timeseries before applying PCMCI+. Here, for example, we show how we mask the data according to the PDV- (top) and PDV+ (bottom) regimes. The grey shaded periods are masked and thus not considered during the PCMCI+ analysis. Note that the masking here refers to variables at time point X_t^j while their lagged parents can originate also from a masked period (gray shaded). This setting is referred to as `mask_type='y'` in Tigramite. Consequently, applying PCMCI+ on differently-masked timeseries produces different causal networks (network in top vs network in bottom)

the gray shaded parts of the timeseries are masked periods, i.e. only the black shaded periods (see timeseries in Figure 3b) are considered. We show in Appendix Table A4 to Table A10, the number of years per regime for each dataset analysed. Nonetheless, it should be stated that the results of the regime-oriented causal analysis account for potential errors related to the sampling of the data. A study from Smirnov and Bezruchko (2012) demonstrated, using a variety of examples, how sampling at lower intervals can produce large "spurious" results.

We note that the low-pass filtered indices are used only to extract the time periods that constitute each regime. We remove any linear trend that might be present in the data prior to applying the causal discovery algorithm. In this way, the effects of external forcings are reduced. The four indices (AMV, PNA, PDV, PSA1) to which PCMCI+ is applied are represented by detrended yearly unfiltered (not smoothed) timeseries (see Figure 2 and Figure 3b).

2.1.4 F_1-scores for causal network comparison

To quantify the similarity between the resulting causal graphs (networks) from model simulations and those from observations, we follow a similar modified F_1-score as in the methods by Nowack et al. (2020). The F_1-score ranges between 0 (no match) and 1 (perfect network match) and is based purely on the existence or non-existence of links in a network relative to a reference network. The F_1-score combines the statistical precision (P, fraction of links in model simulation network that also occur in the reference network) and recall (R, fraction of links in the reference network that are detected in the model simulation network) and is defined as:

$$F_1 = \frac{2 \times P \times R}{P + R}$$

with

$$P = \frac{TP}{TP + FP}$$

and

$$R = \frac{TP}{TP + FN}$$

where FP is the number of falsely detected links and FN is the number of not detected links. We modify the definition as in Nowack et al. (2020) so that a link is considered a true positive (TP) if it is found with the same sign of MCI partial correlation as in the reference network. We further relax the time lag constraint by considering a TP to exist if a link is found in a ± 10 time-step interval compared to the lag in the reference network (i.e. $[min(\tau_{max},\, \tau + 10),\, max(0,\, \tau - 10)]$).

2.2 Data

From the 1900-2014 historical climate variability diagnostic results provided by the CVDP-LE, we choose the SST from the Extended Reconstructed Sea Surface Temperature (ERSST) Version 5 (Huang et al., 2017) by the National Oceanic and Atmospheric Administration (NOAA) as reference for the AMV and PDV indices and spatial patterns. Whereas for the PNA and PSA1 modes, we use as reference, SLP from the 20^{th} Century Atmospheric Reanalysis extended with ERA5

(ERA20C_ERA5), provided by the European Centre for Medium-Range Weather Forecasts (ECMWF) and assimilating observations of surface pressure. The reference data serve for comparison to evaluate how indices generated using a selection of 12 Large Ensemble CMIP6 historical models reproduce the observed spatial patterns and causal dependencies. The list of CMIP6 LE models (with the number of realization per model) is provided in Table 1.

Table 1. CMIP6 Large Ensemble historical simulations used in the analysis

Dataset		**Components**		**N° realisations used**	**References**
CMIP6 LE	**Institute**	**Atmosphere model**	**Ocean model**		
ACCESS-ESM1-5	CSIRO	HadGAM2	ACCESS-OM2	10	Ziehn et al. (2019)
CESM2	NCAR	CAM6	POP2	11	Danabasoglu (2019)
CNRM-ESM2-1	CNRM	Arpege 6.3	NEMO3.6	10	Seferian (2018)
CanESM5	CCCma	CanAM5	NEMO3.4.1	65	Swart et al. (2019)
EC-Earth3	EC-Earth	IFS cy36r4	NEMO3.6	20	Döscher et al. (2022)
GISS-E2-1-H	NASA	GISS-E2.1	HYCOM Ocean	23	Kelley et al. (2020)
INM-CM5-0	INM	INM-AM5-0	INM-OM5	10	Volodin et al. (2019)
IPSL-CM6A-LR	IPSL	LMDZ	NEMO-OPA	32	Boucher et al. (2018)
MIROC6	JAMSTEC, AORI, NIES,R-CCS	CCSR AGCM	COCO4.9	50	Shiogama et al. (2019)
MPI-ESM1-2-LR	MPI-M	ECHAM6.3	MPIOM1.63	10	Wieners et al. (2019)
NorCPM1	NorESM Climate modeling Consortium	CAM-OSLO4.1	MICOM1.1	30	Bethke et al. (2019)
UKESM1-0-LL	Met Office Hadley Centre	MetUM-HadGEM3-GA7.1	NEMO-HadGEM3-GO6.0	18	Tang et al. (2019)

We note that in the spatial correlation analysis in the next section, monthly averages are used for AMV and PDV as that is the time resolution originally provided by the CVDP-LE for these modes. The diagnostic package does not produce monthly fields for the PNA and PSA1, so we use winter means (DJF) and all-year annual means (ANN), respectively. We found that most model simulations show weak correlations with reanalysis data for the annually averaged PNA (ANN, not shown) compared to the winter averaged PNA (DJF, Table 2). Hence, we chose winter means instead of annual means for PNA to reduce any seasonal bias within the simulated spatial patterns. The spatial patterns do not depend much on the time resolution (yearly or monthly) of the data, as they are all calculated on the whole 1900-2014 period. Prior to applying the causal discovery algorithm (Sect. 3.2), however, we yearly average the AMV and PDV timeseries (computed based on monthly means by the CVDP-LE). This way we unify the time resolution of our data to fit the causal analysis by using the yearly resolution to investigate connections on long timescales.

3 Results

3.1 Similarities between the simulated and observed spatial patterns

To accompany the causal analysis, we first calculate pattern correlations (r) for each simulation's SST and SLP regression maps with respect to the reanalysis regression maps (for the complete 1900-2014 period, see Figure 4a). This is to quantify the similarity between the observed and simulated spatial patterns for each of the four modes of climate variability we are to analyse. The purpose is to check if the CMIP6-simulated indices have spatial expressions that resemble those of indices

calculated from reanalysis datasets. To introduce a benchmark of model performance, we calculate a Mean Score for each single simulation by taking the average of the four r values (after applying a Fisher z-transform).

To look closer at how the spatial correlation values spread across every LE and how they differ from one climate variability mode to another, Figure 4b provides a color-coded box-plot showing the distribution of these spatial correlation values, and their respective averages across every Large Ensemble of CMIP6 simulations used in the analysis. It depicts the similarity between the observed (reference maps in Figure 4a) and the simulated patterns from the regression maps for the four modes, with values approaching 1 indicating a better simulation of the patterns associated with the observed modes.

Sorted by the ensemble average mean score of every CMIP6 LE, Table 2 provides a view of the distribution (in the form of minimum, mean, maximum) of spatial correlation values for every mode and their Mean Score for every CMIP6 LE model. It can be seen from Figure 4b and Table 2, based on the ensemble average mean score, that most models perform quite well in simulating the observed geographical patterns of the four indices in Figure 4a, with pattern correlations mostly above 0.75. The UKESM1-0-LL (0.80), MIROC6 (0.80), MPI-ESM1-2-LR (0.79), ACCESS-ESM1-5 (0.77) and CanESM5 (0.77) outperform the other CMIP6 LEs in terms of recreating the spatial patterns of the four selected modes of climate variability. The number of ensemble members within every LE has no apparent effect on the spread of the r value distribution across the models. For example, UKESM1-0-LL and MIROC6 with 18 and 50 realizations respectively, share similar narrow interquartile ranges (IQR, the width between the 3rd and 1st quartiles) of r values for the four climate variability spatial patterns. Appendix Table A1 shows the distribution of Pearson r correlation between observed and simulated spatial patterns of PNA, PSA1, PDV, and AMV from a 10th, 50th, 90th percentile perspective. Looking only at the mean score spread, Table A1 shows the 10th-90th percentile value range is 0.78-0.83 for UKESM1-0-LL, and 0.77-0.82 for MIROC6. This means that most members of these two model ensembles agree between each other and show high spatial similarity with observations when simulating the four modes. It can be concluded that the models generally do a good job in simulating the geographical patterns of the different modes but with different precision. Although the models with high mean scores tend to display high pattern correlations with observations for the four modes of climate variability, the white scatter points on Figure 4b imply that they simulate the PNA (purple) atmospheric mode slightly better than its South Pacific counterpart, the PSA1 (cyan) when compared to the ERA20C_ERA5 reference patterns. These high scoring models, notably UKESM1-0-LL, MPI-ESM1-2-LR, MIROC6, CanESM5 and IPSL-CM6A-LR also, on average, simulate better PDV (red) monthly spatial patterns compared to AMV (green), with ERSSTv5 as a reference dataset for the 1900-2014 period. The mean scores of CESM2, GISS-E2-1-H and NorCPM1 are strongly affected by the low correlation coefficients obtained for the PSA1 mode (cyan boxes). The 50th percentile bar on the cyan box for CESM2 suggests that there are more members with PSA1 patterns resembling the observed ones. The opposite is true for the GISS-E2-1-H model which contains less realizations with similar PSA1 patterns as those from reanalysis. The length of the cyan box for NorCPM1 indicate that most members fail to represent the spatial patterns of PSA1.

Along with the release of the CVDP-LE (Phillips et al., 2020), CESM's CVCWG freely distributes results from several CMIP simulations including the CMIP6 1900-2014 historical simulations, from which data used in this analysis have been downloaded. The results include a pattern correlation summary with 11 key spatial metrics of oceanic and atmospheric modes of variability. Similar to the mean score we introduced in the spatial correlation analysis above, the CVDP-LE provides a mean

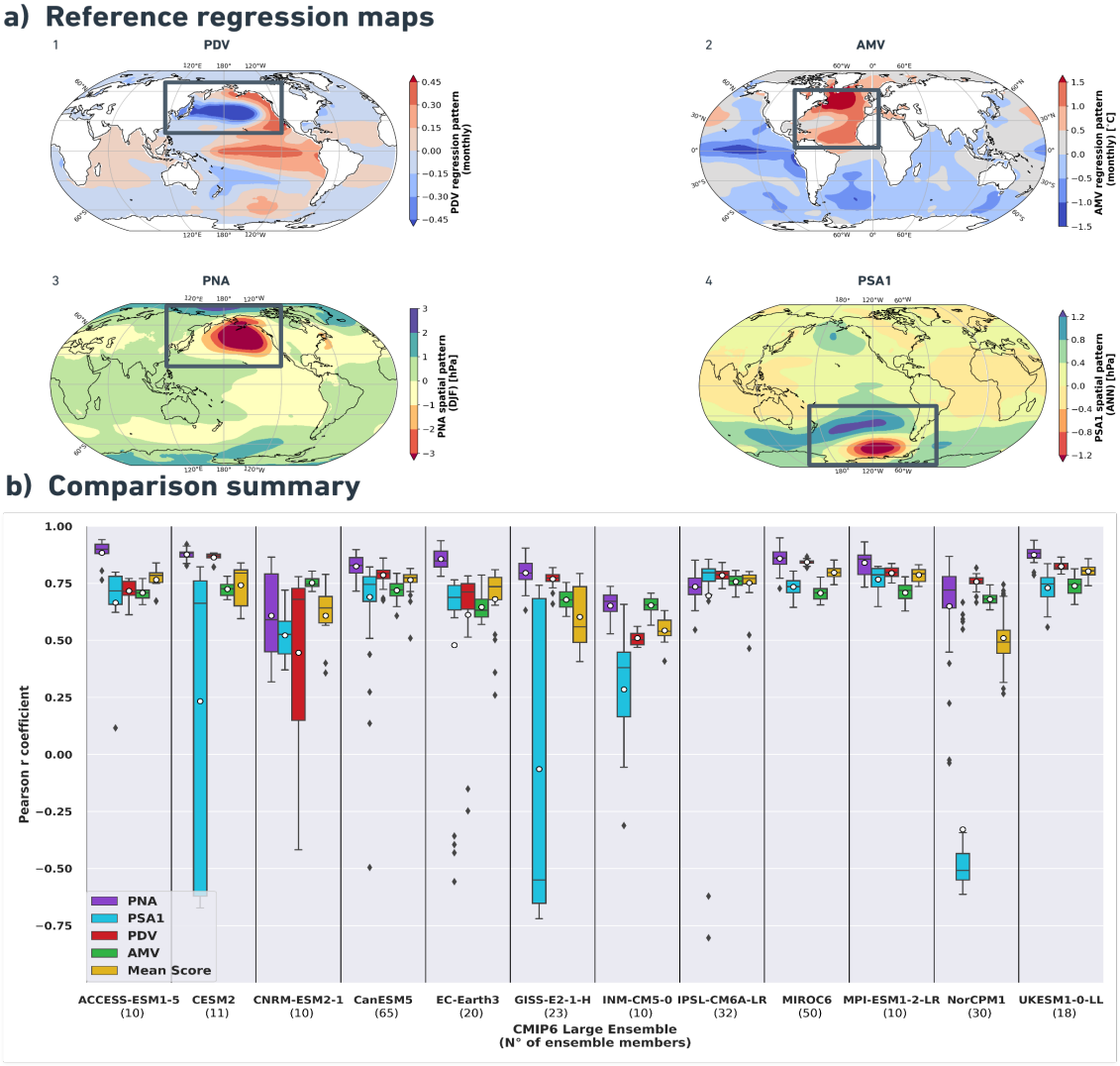

Figure 4. a) Reference for comparison: SST regression maps showing geographcial patterns associated with PDV (1) and AMV (2) and SLP regression maps of geographical patterns associated with PNA (3) and PSA1 (4). The indices are calculated from reanalyses data (ERSSTv5 for AMV and PDV; ERA20C_ERA5 for PNA and PSA1) over the 1900-2014 period using the NCAR CVDP-LE package. Rectangles on the maps approximate the regions over which the indices are defined (see Methods, Sect. 2.1.1). b) Box-plot (or whisker-plot) showing the distribution of Pearson r pattern correlation values along the different historical CMIP6 LEs (between parenthesis on the x-axis is the number of ensemble members within each model). The bottom of every box (color-coded part) shows the first quartile (Q1 or 25th percentile), the top the third quartile (Q3 or 75th percentile) and the horizontal bar between them denotes the median value (Q2 or 50th percentile). The length of the box (from Q1 to Q3) denotes the interquartile range (IQR) while the bottom and upper whiskers (thin lines extending from boxes) extend to the minimum and maximum values, which are calculated as Q1-1.5*IQR and Q3+1.5*IQR, respectively. The black dots are outliers. PNA correlation values are shown in purple, PSA1 in cyan, PDV in red and AMV in green. Yellow boxes show the Mean score denoting the average of the four r values (after applying a Fischer z-transform). White dots denote the mean value.

Table 2. Pearson r correlations between the simulated (CMIP6 LE) and observed (ERA20C_ERA5, ERSSTv5) spatial patterns of PNA, PSA1, PDV and AMV over the 1900-2014 period. Models are sorted according to the average mean score (column in bold; descending order).

CMIP6 LE	Mean Score			PNA (DJF)			PSA1 (ANN)			PDV (monthly)			AMV (monthly)		
	min	**mean**	max	min	mean	max	min	mean	max	min	mean	max	min	mean	max
UKESM1-0-LL	0.74	**0.80**	0.86	0.79	0.87	0.94	0.56	0.73	0.84	0.79	0.82	0.86	0.66	0.74	0.81
MIROC6	0.74	**0.80**	0.85	0.73	0.86	0.95	0.64	0.73	0.80	0.82	0.84	0.87	0.66	0.71	0.78
MPI-ESM1-2-LR	0.74	**0.79**	0.83	0.73	0.84	0.93	0.65	0.77	0.82	0.75	0.80	0.84	0.63	0.71	0.78
ACCESS-ESM1-5	0.67	**0.77**	0.84	0.76	0.88	0.94	0.12	0.67	0.80	0.61	0.72	0.77	0.66	0.71	0.77
CanESM5	0.51	**0.77**	0.81	0.71	0.82	0.90	-0.50	0.69	0.82	0.67	0.79	0.86	0.61	0.72	0.79
IPSL-CM6A-LR	0.46	**0.75**	0.80	0.55	0.73	0.85	-0.80	0.70	0.86	0.73	0.78	0.84	0.69	0.76	0.81
CESM2	0.59	**0.74**	0.84	0.83	0.88	0.92	-0.67	0.23	0.82	0.82	0.86	0.88	0.68	0.72	0.78
EC-Earth3	0.26	**0.68**	0.81	0.78	0.86	0.94	-0.56	0.48	0.76	-0.25	0.61	0.78	0.57	0.65	0.79
CNRM-ESM2-1	0.36	**0.61**	0.79	0.32	0.61	0.86	0.37	0.52	0.72	-0.42	0.45	0.78	0.71	0.75	0.80
GISS-E2-1-H	0.41	**0.60**	0.79	0.63	0.80	0.90	-0.72	-0.06	0.74	0.66	0.77	0.82	0.60	0.68	0.75
INM-CM5-0	0.41	**0.54**	0.63	0.53	0.65	0.74	-0.31	0.28	0.66	0.47	0.51	0.56	0.57	0.65	0.71
NorCPM1	0.27	**0.51**	0.74	-0.04	0.65	0.87	-0.61	-0.33	0.67	0.67	0.76	0.82	0.63	0.68	0.74

score averaging the pattern correlations of the 11 metrics used. Although the pattern correlation mean score we calculated is not exactly the same as the one provided by the CVDP-LE tool because the number of indices used is different (four vs 11), the highest-scoring CMIP6 LEs from Table 2 (UKESM1-0-LL, MIROC6 and MPI-ESM1-2-LR) were also the highest scoring ensembles according to the pattern correlation summary provided on the tool's repository (Phillips et al., 2020). Moreover, one simulation from the UKESM1-0-LL ensemble, the r19i1p1f2 realization, was found to obtain the highest mean score based on both the pattern correlation values published under https://webext.cgd.ucar.edu/Multi-Case/CVDP-LE_repository/CMIP6_Historical_1900-2014/metrics.html by CVDP-LE authors (Phillips et al. 2020, 0.88 using 11 indices) and our calculations in Table A2 (0.86 using 4 indices)

3.2 Regime-oriented causal analysis of observations and reanalyses

Several mechanisms are hypothesized to contribute to PDV and AMV. PDV is initially considered as a mode of internal climate variability (e.g. Meehl et al., 2021b). However, previous research indicates possible external contributions in the form of solar (Meehl et al., 2009), greenhouse gas (Meehl et al., 2009; Fang et al., 2014; Dong et al., 2014) or volcanic and anthropogenic aerosol forcings (Wang et al., 2012; Maher et al., 2015; Smith et al., 2016; Takahashi and Watanabe, 2016). There are studies suggesting that such external anthropogenic aerosol forcing might be contributing to AMV as well (Booth et al., 2012; Zhang et al., 2013; Si and Hu, 2017), but evidence from Zhang et al. (2019) supports the notion that the AMV is primarily linked to internal variability of the Atlantic Meridional Overturning Circulation (AMOC) and its associated meridional heat transport.

This means that the fingerprint of any possible external forcing acting as a confounder is embedded in the timeseries information of the extracted indices of the modes of climate variability used in this study. The linear detrending we perform prior to applying PCMCI+ will at least partially reduce such effects. However, as mentioned before, the subtraction of the global mean temperature for PDV and AMV and the linear detrending of all time series do not address local, nonlinear effects, which could be related to the aerosol forcing that varies over time and space. It is then important to recall that in this paper, the indices do not represent a fully isolated internal variability component but rather a mixture of naturally-occurring internal variability and nonlinear effects of external forcing, mainly in the form of aerosol forcing.

PCMCI+ is applied first to the indices of PDV, AMV, PNA and PSA1 calculated from reanalysis data, as a proxy for observations, to reveal any causal dependencies between the modes depicted by the observed timeseries information. As it is assumed that the nature of teleconnections between the different climate variability modes can vary over decadal timescales depending on the different phases these modes go through, we mask years of data (as discussed in Sect. 2.1.3) to reveal the causal structures during specific periods (regimes) in time. Reference causal networks obtained by running PCMCI+ on reanalysis data for the different regimes are shown in Figure 5.

The results show that the causal dependencies (links) between the four modes of climate variability (nodes) change from one regime to another. Starting from an analysis on the complete period (115 years, upper left panel in Figure 5, and see Table A3 for exact cross-MCI values of the complete period causal graph) PCMCI+ reveals four different links: An 11-year lagged negative (link arrow is curved and blue) AMV→PDV link (cross-MCI = -0.25) showing that the opposite sign effect on PDV caused by AMV is lagged by a decade (e.g. positive AMV tends to produce negative PDV about a decade later). Therefore, this link can be interpreted as lagged opposite sign SST anomaly changes over the Pacific in response to SST anomaly changes over the Atlantic. The same causal graph features a strong positive (0.53) contemporaneous PDV—PNA link (i.e. link line is straight) suggesting PDV is strongly associated to PNA. In addition, the complete period graph implies weak South Pacific teleconnections of both AMV and PDV which are represented by a positive contemporaneous AMV—PSA1 (0.25) link and a lagged PSA1→PDV link. The latter (PSA1→PDV link) is detected positive at 7 years (0.23) and negative at 15 years (-0.31). As explained in Sect. 2.1.2, if a lagged link is found at more than one time lag, the causal graph shows the link at the lag when it is most significant (i.e higher absolute cross-MCI value) and labels the other time lags after a comma ($|-0.31|$ vs $|0.23|$ in this case, thus the "15, 7" label on the PSA1→PDV link; see upper left panel in Figure 5).

The complete period graph in the upper left in Figure 5 is useful to show the causal dependencies happening throughout the whole observational record used. However, this methodology can also be used to look at specific regimes to notice the change in dependencies arising from the physical state of the Atlantic and Pacific basins during those time periods. For example, the causal graphs from PDV+ and PDV- regimes indicate that direct decadal AMV—PDV interactions occur only during the PDV- regime (third row, left panel in Figure 5), whereas during the PDV+ regime (second row, left panel in Figure 5) we find a contemporaneous atmospheric teleconnection from PNA to both AMV and PDV. This difference could be explained by the fact that the PDV- regime comprises two important Atlantic variability events: the 1920s AMV phase-switch from negative to positive (see dashed lines showing low-pass AMV in Figure 3a) and the subsequent switch from positive back to negative during late 1960s.

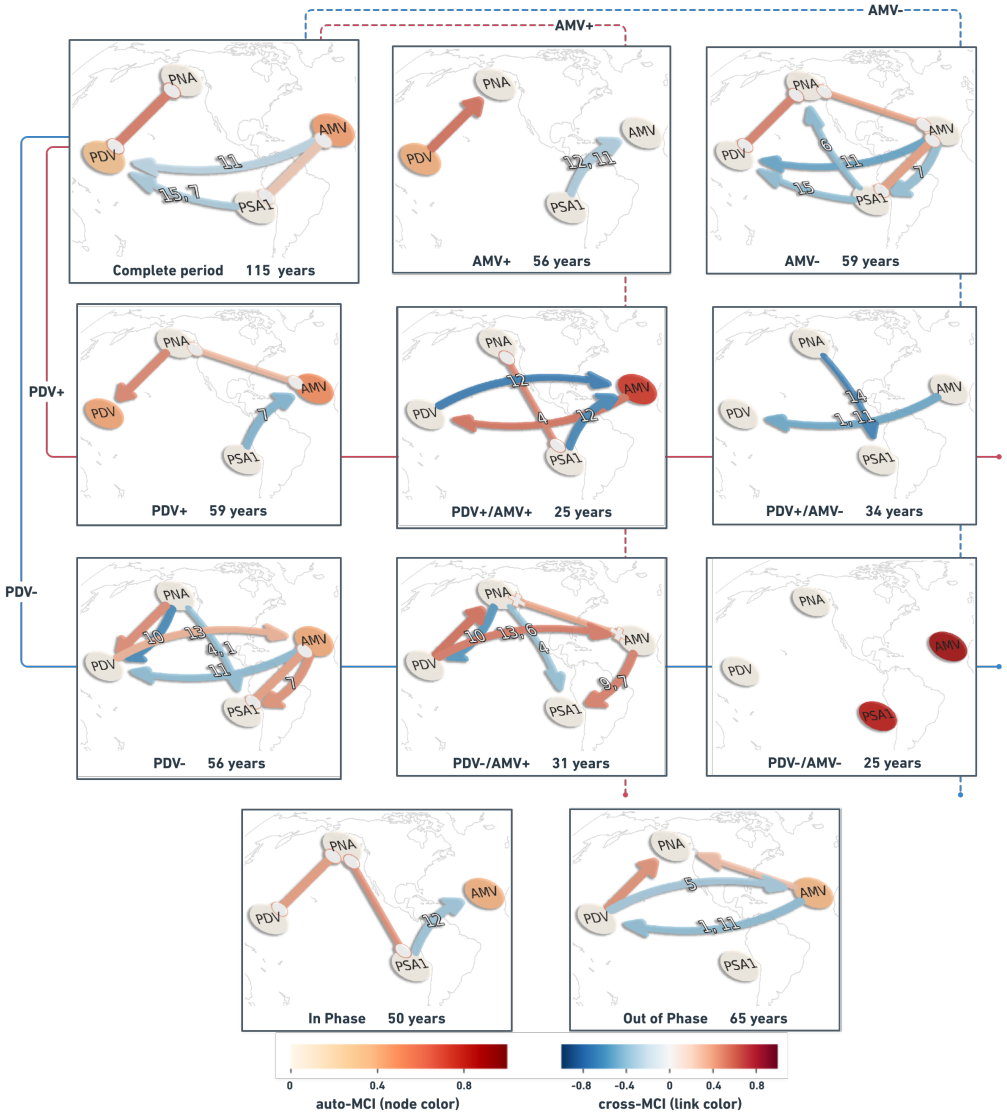

Figure 5. Causal networks calculated with PCMCI+ from reanalysis data for the complete 1900-2014 period (upper left panel) and the different regimes. Nodes represent the timeseries associated with each climate variability index (see node labels) masked according to the predefined regimes. Node colours indicate the level of autocorrelation (auto-MCI) as the self-links of each node with darker red indicating stronger autocorrelations (color bar at lower left) while the color of the arrows (termed "links" here) denotes the inter-dependency strength (cross-MCI) with blue indicating opposite-sign (or negative) inter-dependency and red indicating same-sign (or positive) inter-dependency strength (color bar at lower right). Small labels on the curved links indicate the link-associated time lags (unit = 1 year). Straight links show contemporaneous inter-dependencies happening with no time lag (i.e. $\tau < 1$). Each network is sub-labeled with its respective regime name and the total number of unmasked years (time-steps) that characterize that regime (label and number of years at bottom of each panel). Lines going through the panels are to help visualize which combinations make up the regimes. Solid lines are for PDV, dashed for AMV. Red for warm (+), blue for cold (-) phases (e.g. PDV+/AMV- regime panel has a solid red line and dashed blue line going through it).

The regime-oriented nature of this causal analysis provides for a separation of signals, for example delineating the PDV+ regime that depends on the AMV phase during those 59 years (second row panels in Figure 5). The short length of timeseries, in addition to the time-varying aerosol forcing during such regimes, can lead to inconclusive causal estimations. The PDV-/AMV- panel at the right of the third row in Figure 5 (25 years) shows strongly auto-correlated AMV and PSA1 patterns but no apparent links between any of the four variables. However, these short regimes might also reveal interesting causal relations that are not apparent when analysing longer periods. This is the case for the causal graph from the 25 years of the PDV+/AMV+ regime (central panel in Figure 5), which is the only one to feature a strong negative PDV→AMV link and a positive AMV→PDV link with comparable strength. Since the causal parents that drive the variables (other variables or the same one at different past time-steps) can originate from a masked period with respect to τ_{max}, it implies, for example, that the strong 12-year lagged negative PDV→AMV causal link estimated during the PDV+/AMV+ regime (second row, central panel in Figure 5), might have fingerprints originating from a previous regime.

The limitation presented by the fact that some regimes might be too short to detect any causal links (e.g. PDV-/AMV-, 25 years) is overcome when introducing causal graphs for In-Phase and Out-of-Phase regimes (panels in the bottom of Figure 5). As explained in Sect. 2.1.3, the In-Phase regime is made up of the time-steps where AMV and PDV happen to be on the same phase (PDV+/AMV+ and PDV-/AMV-) while the Out-of-Phase regime is composed of time-steps where the two modes are on opposite phases (PDV+/AMV- and PDV-/AMV+), resulting in longer regime periods. We detect the negative lagged direct AMV→PDV and PDV→AMV only during the Out-of-Phase regime with a strong positive extra-tropical PDV→PNA teleconnection and a weaker AMV→PNA teleconnection. The In-Phase regime features a fast (zero lag) PDV teleconnection to PNA, PNA connection to PSA1, and a 12-year lagged PSA1→AMV link. As finite sample errors can lead to false positives as well as false negatives (missing links), it is difficult to attribute a physical explanation to every detected link. Though here both are thought to be driven by tropical precipitation and heating anomalies, we refrain from assigning any processes that might be behind the direct PNA—PSA1 causal links due the lack of knowledge regarding possible direct links between the North Pacific and South Pacific extra-tropics.

Through observations of the long-term variability patterns and pacemaker simulations of Atlantic and Pacific ocean basins, Meehl et al. (2021a) explain how positive AMV could produce an opposite-sign response, mainly through the atmospheric Walker circulation, leading to negative PDV, and then the negative PDV subsequently contributing a same-sign response in the Atlantic driving the AMV from positive to negative phase. This mutual contrasting response from one basin to the other can be interpreted through the blue (negative cross-MCI) lagged AMV→PDV links and the reddish (positive cross-MCI) lagged PDV→AMV links in the causal networks in Figure 5. The results in Figure 5 show that the lagged AMV→PDV causal link has been estimated over the complete period and during five out of the 10 regimes (AMV-, PDV-, PDV+/AMV+, PDV+/AMV-, Out-of-Phase). During four of these regimes, the link can be interpreted as a lagged opposite-sign effect of AMV on PDV (blue curved link). The study of Meehl et al. (2021a) suggests that in addition to the tropical Walker circulation, positive convective heating and precipitation anomalies in the tropical Pacific establish extra-tropical teleconnections to PNA and PSA which contribute to the same-sign effect of PDV on AMV. The causal graph from the 31 years of the PDV-/AMV+ regime (third row, middle panel in Figure 5) shows two possible pathways for this same-sign effect of PDV on AMV. During that

regime, PCMCI+ estimates a strong positive 13- and 6-year lagged PDV→AMV link (the 13-year lagged link was also found during the 56 years of the PDV- regime) but also shows a positive PDV→PNA—AMV contemporaneous teleconnection where PNA seems to mediate the same-sign effect of PDV on AMV. Therefore, this analysis presents additional evidence that AMV (although potentially affected by a forced aerosol signal) might serve as a predictor of decadal variability over the Pacific (hence for PDV) and eventually the other way around (d'Orgeville and Peltier, 2007; Zhang and Delworth, 2007; Chikamoto et al., 2015; Johnson et al., 2020).

An earlier study from Zhang and Delworth (2007) proposed a mechanism in which positive (negative) AMO would lead to high (low) SLP anomalies over the North Pacific and eventually a positive (negative) PNA pattern. This weakening (strengthening) of the Aleutian low associated with the PNA pattern projects onto the multidecadal mode of variability over the North Pacific. The response of North Pacific SST to the anomalous PNA pattern induced by AMO is hypothesised to be lagged due to Rossby wave propagation and gyre adjustment where the authors found a 3-year lag when using a model simulation compared to a 12-year lag when they analysed the observed pattern. The extra-tropical contributions of PNA and PSA1 on the mutual PDV—AMV interactions can be concluded from causal graphs constructed during different regimes (see Figure 5). AMV-, PDV+, PDV-/AMV+ and Out-of-Phase are all regimes that suggest mutual Atlantic-Pacific connections can be established via PNA. The causal networks from the complete period and AMV- regime show that these inter-basin connections can also happen through PSA1.

Previous research also showed that components of the PDV can be forced by tropical Pacific variability and/or driven by atmospheric stochastic forcing which are both closely tied to Aleutian low variability associated with the PNA pattern (Newman et al., 2016; Johnson et al., 2020). This literature finding on the PDV—PNA teleconnection validates the contemporaneous PDV—PNA causal link estimated by PCMCI+ during most regimes (all except PDV+/AMV+ and PDV-/AMV-; see causal networks in Figure 5) with a strong positive cross-MCI value. The link is directed in some regimes (straight links with arrowhead, e.g. during PDV+ regime) while it is unoriented during other regimes (straight links with no arrowheads, e.g. during AMV- regime). A 10-year lagged negative PNA→PDV link appears during the PDV- regime in Figure 5 (and during PDV-/AMV+) which suggests that an extra-tropical teleconnection to PNA might have the opposite effect during longer time lags.

Generally, lags ranging from interannual (1 to 5 years, Wu et al., 2011; Meehl et al., 2021a) to decadal (12 to 17 years, Wu et al., 2011; Chylek et al., 2014) timescales have been proposed by previous studies for Atlantic-Pacific interactions which fall in the same range of time lags at which causal links have been estimated by PCMCI+ in this study.

To further justify the credibility of the constructed causal networks, we use the estimated causal graph from the complete period to construct a model that explains the lagged correlation structure of the reanalysis dataset. This is done by fitting a linear structural causal model to causal parents taken from the original reanalysis causal graph. We generate 100 realizations following a linear Gaussian causal model with the noise structure estimated from the noise covariance matrix of residuals. Figure 6 shows lagged correlations of the original data in red with the mean lagged correlations from the synthetically generated data in black and their 5th-95th percentile range in grey. The original lagged correlations (red) fall mostly within the 90% range (with the clear exception of AMV's lagged auto-correlation at the upper left of Figure 6). This means that a linear Gaussian model with the same links as those from the reconstructed causal graph can well explain the whole lagged correlation structure of the

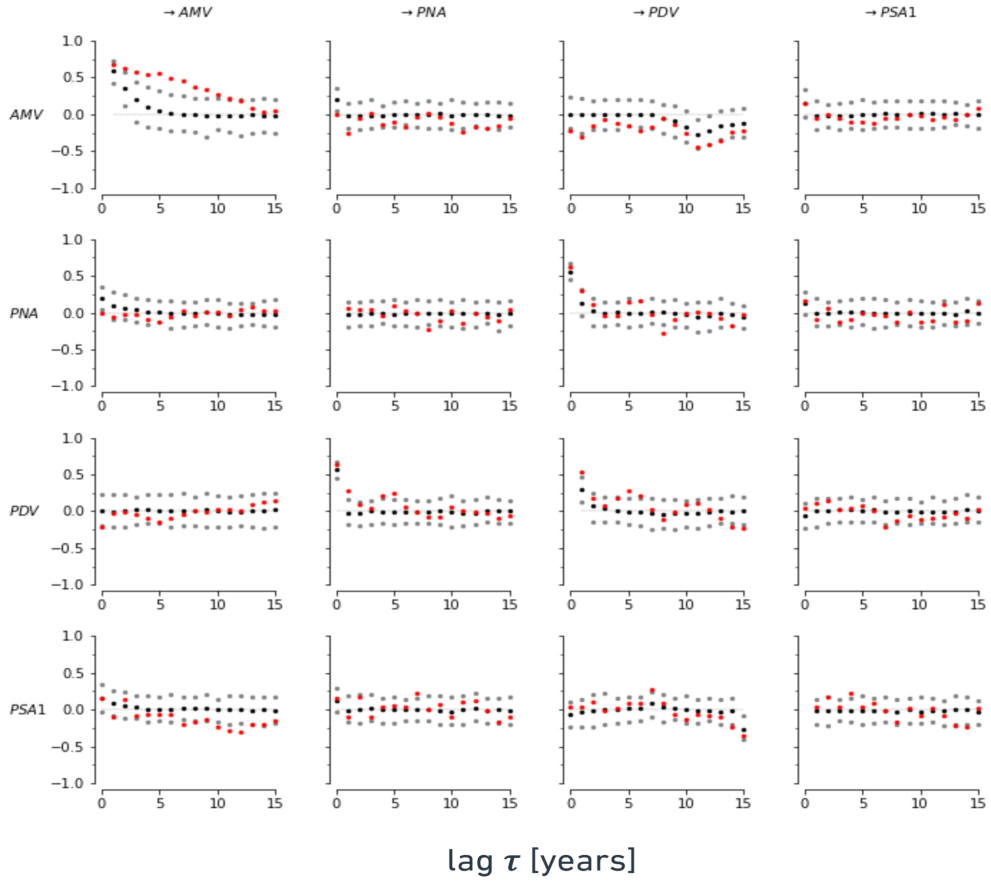

Figure 6. Lagged correlations of original data (lag in years, complete period graph from reanalysis data) in red shown together with lagged correlations of an ensemble of synthetic data generated by a linear Gaussian structural causal model with causal coefficients and noise structure estimated from the original data. The mean lagged correlations from the synthetically generated data are shown in black, and their 5th-95th percentile range in grey. X-axis shows lag in years.

original data for PNA, PDV and PSA1. Such a lagged-correlation matrix (Figure 6) also unveils how the dependencies between different variables change over time.

3.3 Regime-oriented causal model evaluation of the CMIP6 Large Ensembles

With the overall high level of fidelity that several models show in simulating the spatial patterns of at least the major modes of climate variability presented in this paper (see Figure 4b), it is crucial to test whether these simulations also account for the possible lagged causal pathways between these different modes. To benchmark the dependency structures in model simulations, the simulated causal graphs are compared to those from reanalysis datasets (ERSSTv5 for PDV and AMV, ERA20C_ERA5 for PNA and PSA1). The constructed causal graphs from the previous section illustrate the connections occurring between the

different modes of climate variability during different regimes, as estimated from reanalysis data. Relative to reanalysis, we consider the causal graphs from Figure 5 as reference for the CMIP6 model evaluation to be demonstrated in this section.

The exact same PCMCI+ setting (see Methods; Sect. 2.1.2 and Sect. 2.1.3) used in the section above is applied for timeseries indices calculated from every realization of the CMIP6 models listed in Table 1. In Sect. 3.1, we found that, overall, the spatial patterns of these simulated indices compare fairly well to the observed ones (Figure 4, Table 1). The purpose of this section is to show how the causal fingerprints in these simulations compare to those observed. For every realization, the analysis is run for the complete period in addition to the 10 different regimes, similar to the regime-oriented setting on reanalysis data in the section above. As the PDV and AMV phases occur in model simulations at different time periods than those in reanalysis (due to randomly generated internal variability and time-varying forcing caused mainly by aerosols), models need not show similar networks for the same periods as in observations. However, we can assess the degree of similarity in the causal fingerprint that these simulations hold within their modeled dynamics. The results of every realization during every regime are compared to the reference networks from reanalysis data during that regime.

To illustrate results from an individual model, we aggregate causal networks from 65 realizations from the CanESM5 model in Figure 7. This figure shows networks with links of variable thickness indicating that some links are found in most ensemble members during that specific regime (thick links, e.g. PDV—PNA in most regimes) compared to other links (thinner links, e.g. PDV→AMV in most regimes) which were detected only by a small fraction of ensemble members. The thicker the link, the more agreement between members of the same ensemble in detecting that specific link. We also label the links with the rounded mean lag at which they are detected in the ensemble members. The link color in this ensemble summary (Figure 7) is informative of the level of agreement between ensemble members in estimating that causal link with the same sign. The clearer the shade of blue (negative) or red (positive), the better agreement between ensemble members in simulating the link with the same sign. For example, the color of AMV—PNA links in most regimes (although mostly estimated by few members during each regime, i.e. relatively thin links; see Figure 7) tend towards reddish shades suggesting that the CanESM5 members, in which such links were estimated, agree that the causal link is of positive sign. This can be translated to the positive (negative) AMV driving positive (negative) PNA and vice versa. This can be seen on all causal networks in Figure 7, except the ones from PDV+/AMV+ and PDV-/AMV+ regimes indicating that in a few of the CanESM5 realizations, AMV would induce an opposite sign response on PNA (see thin blue AMV→PNA links on PDV+/AMV+ and PDV-/AMV+ causal graphs in Figure 7).

Other than the PDV—PNA links (estimated by most ensemble members during all regimes), the occurrence of a link in the CanESM5 model seems to vary from one regime to another. This is less true for the complete period, the In-Phase and the Out-of-Phase regimes. The complete period ensemble causal graph distinctly shows AMV—PNA interactions as same-sign causal links between the two modes. The same graph (upper left panel in Figure 7) also shows a clear blue AMV→PDV link, demonstrating the opposite-sign response driven by AMV on PDV, similar to the one featuring in the complete period causal graph from reanalysis data (upper left in Figure 5). The color and width (thickness) of this AMV→PDV link in the complete period graph in Figure 7 (upper left panel) suggest that the link was estimated with negative cross-MCI values by a considerable fraction of CanESM5 simulations.

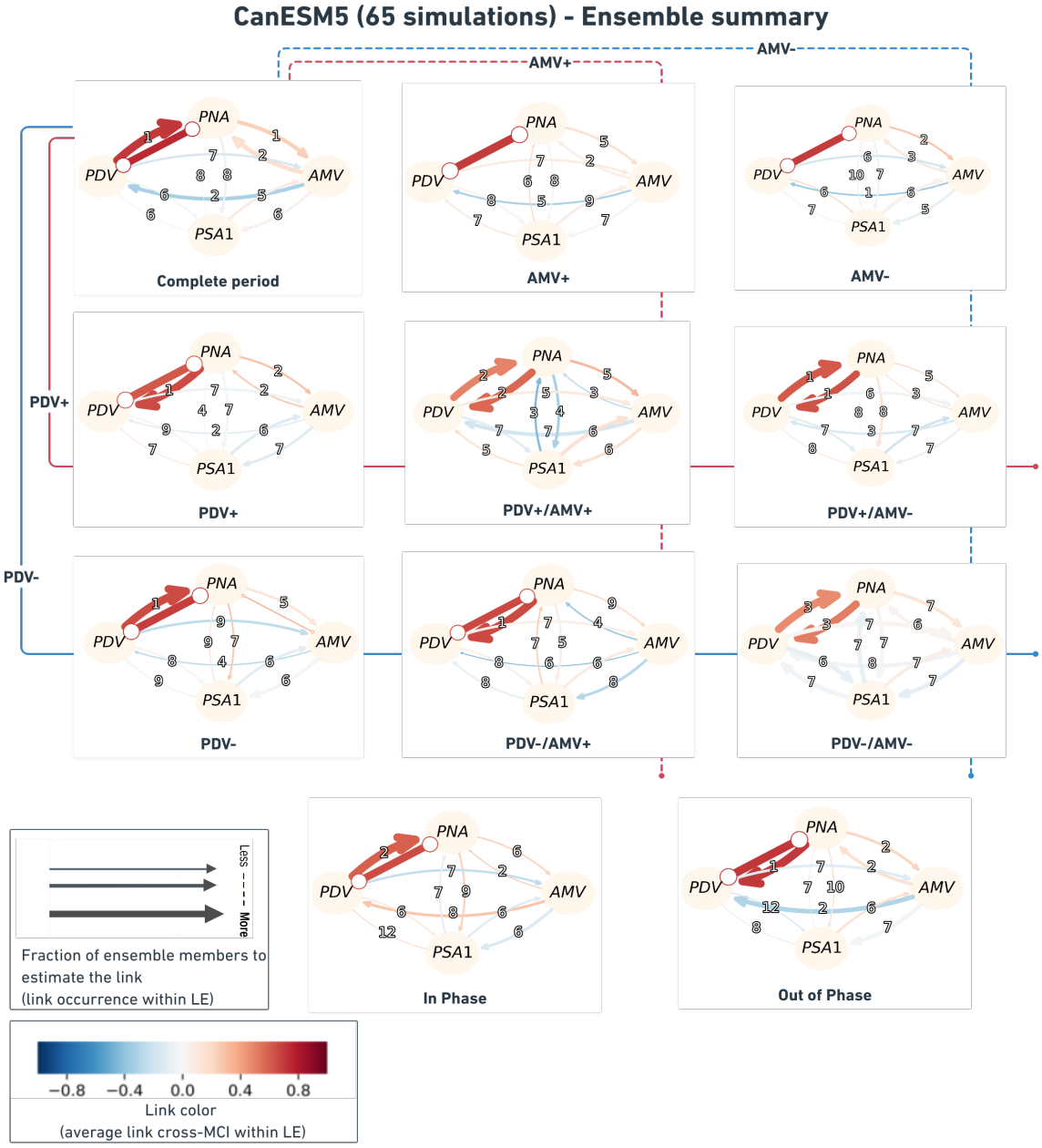

Figure 7. Ensemble summary of the CanESM5 LE model. Similar to Figure 5, but aggregating causal networks from 65 realizations. The link width here shows the fraction of ensemble members that feature that link relative to the total ensemble size (here 65); i.e. the thicker the link, the more ensemble members were found to estimate it during that specific regime. Link colors here translate the mean cross-MCI value among the ensemble members that estimated such link (color bar at lower left). Links of very light color are those that ensemble members agree little on their partial correlation sign. The link labels indicate the average time lag (rounded to the nearest integer) at which the link is estimated among the fraction of ensemble members that find such link.

A more evident network similarity is evinced during the Out-of-Phase regime. Both the graph from reanalysis (Figure 5, Out-of-Phase) and the CanESM5 ensemble graph (Figure 7, Out-of-Phase) display a short lagged (1-year lag and 2-year mean lag, respectively) opposite-sign (blue, negative cross-MCI) AMV→PDV causal link. Moreover, the two graphs (Out-of-Phase causal networks in Figure 5 and Figure 7) suggest a same-sign (red, positive cross-MCI value) contemporaneous and short-lagged (1 year) PDV—PNA causal links, and weaker same-sign (lower positive cross-MCI values) AMV—PNA links. The latter links are instantaneous in the reanalysis data but lagged in CanESM5. However, the short mean lag (2 years) in the simulated CanESM5 Out-of-Phase graphs imply that several members estimate a contemporaneous link.

The CanESM5 ensemble causal graph during the In-Phase regime at the bottom of Figure 7 demonstrates the advantage of using LEs. While the reanalysis graph during this regime suggests only PDV—PNA and lagged PSA1→AMV teleconnections (with a debatable contemporaneous PNA—PSA1 link), the CanESM5 ensemble graph displays a clear same-sign lagged AMV→PDV link with a third of its ensemble members simulating such a dependency. Despite the fact that the positive AMV→PDV link is not detected in reanalysis during the In-Phase regime (Figure 5, In-Phase regime causal graph), literature supports this contrasting effect estimated by CanESM5 model data (Wu et al., 2011; Meehl et al., 2021a). Model simulations can therefore explain causal dynamics between modes of climate variability that might not definitively appear when analysing observations. There is less doubt about the agreement between members of the CanESM5 ensemble, and also when compared to reanalysis, about the occurrence of an AMV→PDV link with an opposite sign during the Out-of-Phase regime.

Ensemble summary plots are calculated for all CMIP6 LEs from Table 1 but we only chose to display them for CanESM5 in Figure 7. The ensemble summary of causal networks from reanalysis data and the 12 CMIP6 models for the complete 1900-2014 period, Out-of-phase and In-Phase regimes are shown in appendix Figs. A1-A3 respectively. In order to measure the level of similarity between observed and individual ensemble member networks across all the CMIP6 models, F_1-scores are computed for every realisation and every regime. The results reveal that most CMIP6 Large Ensembles show better network (causal graph) similarity with reanalysis reference networks during the Out-of-Phase regime, compared to the networks drawn during the other regimes and/or the complete period. The whisker plot in Figure 8a shows the distribution of F_1-scores across the CMIP6 LEs for the complete period (light blue boxes), the In-Phase regime (dark blue) and the Out-of-Phase regime (green). The range of scores during the other regimes (not shown) was found to be much lower compared to the scores during the regimes shown in Figure 8a. The white scatter points show that on average, CESM2, CanESM5, MIROC6 and MPI-ESM1-2-LR LEs clearly display better network similarity with observations during the Out-of-Phase regime. The highest scores during this regime (0.92) belong to members of CanESM5 and MIROC6 LEs (see location markers on whisker plot). Figure 8b compares Out-of-Phase causal graphs from these highest-scoring realizations (and their low-pass filtered AMV, PDV timeseries) to those from reanalysis. The networks in Figure 8b agree on the 1-year lagged AMV→PDV link. The positive contemporaneous PDV—PNA link is directed differently in reanalysis and CanESM5 r11i1p2f1, but unoriented in CanESM5 r17i1p2f1 and MIROC6 r20i1p1f1. The Out-of-Phase graphs from these realizations also agree on a same-sign contemporaneous AMV—PNA dependency, with a lower cross-MCI value (weaker) than that of the PDV—PNA connection.

In Figure 9 we perform intra- and cross-model network comparisons for the complete period and long regimes. This is done by computing F_1-scores with every single realization as a reference. Averaging the F_1-scores by ensemble produces an

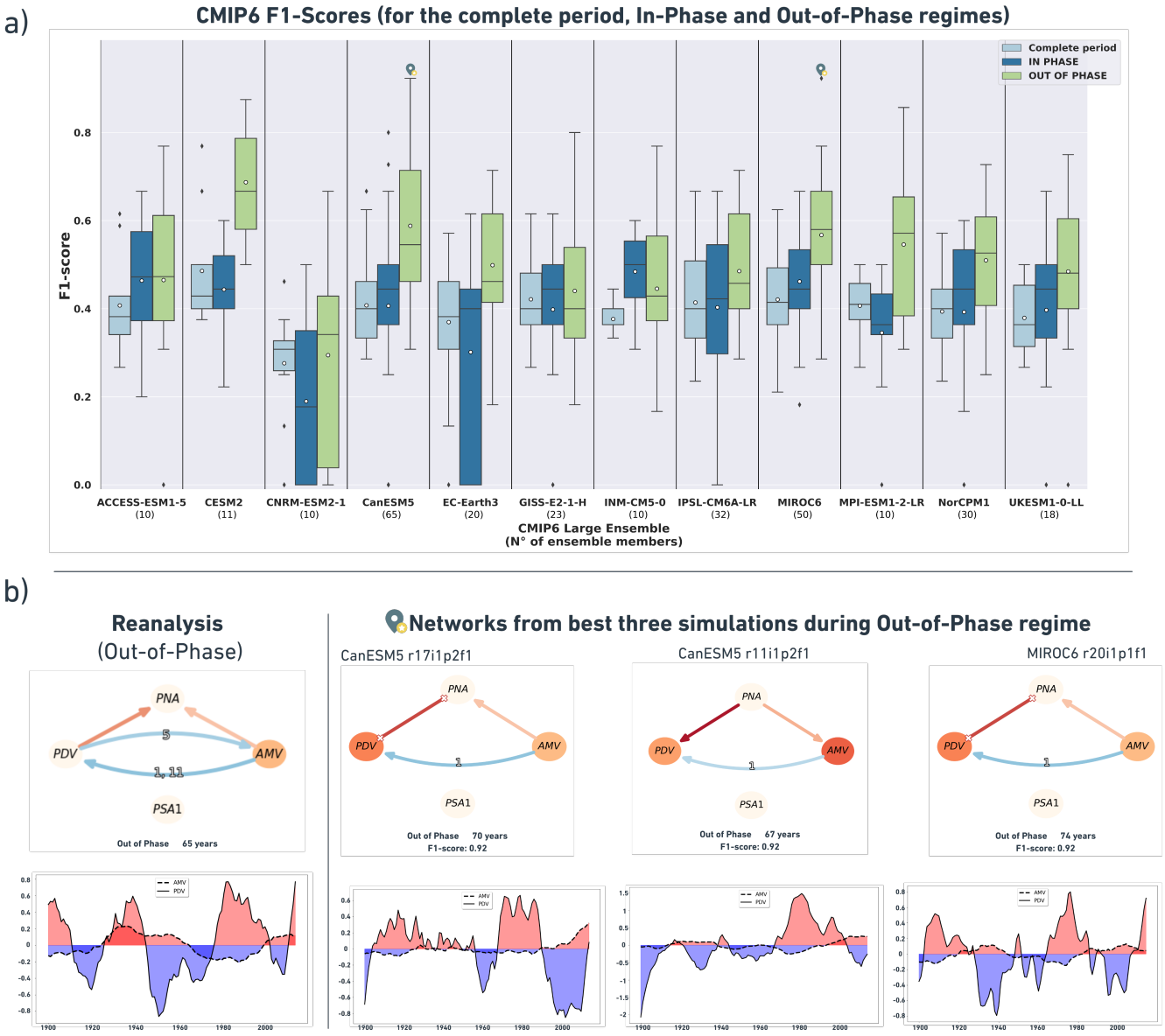

Figure 8. a) Whisker plot showing the distribution of F_1-scores across the CMIP6 LEs for the causal analysis for: the complete period (light blue boxes), the In-Phase regime (dark blue boxes) and the Out-of-Phase regime (green boxes). White scatter points denote the mean LE F_1-scores. b) Reference causal network estimated from reanalysis during the Out-of-Phase regime (left, with low-pass AMV and PDV timeseries below) compared to networks and timeseries from three CMIP6 simulations (right, with simulated low-pass AMV and PDV timeseries below each network) with the best network similarity i.e. highest F_1-score.

F_1-matrix for every regime in the form of heat maps translating the degree of similarity (the redder the color, the greater the similarity) in causal dynamics between members of the same LE (boxes on the main diagonal) and pairwise causal similarity between different LEs (boxes outside the main diagonal). Every grid box on the heat maps shows how the corresponding CMIP6 model from the axis on top (see model names on x-axis top of every panel) compares to the reference corresponding CMIP6 model (see model names on y-axis left of each panel). We exclude the short regimes (PDV+/AMV+, PDV+/AMV-, PDV-/AMV+ and PDV-/AMV-) from this comparison as the PCMCI+ results during these regimes tend to be inconclusive (i.e. the regimes are too short to estimate any causal link for several simulations from different models). The heat maps show that CNRM-ESM2-1 LE clearly stands out as the most dissimilar model during most regimes. This is seen in the third row and third column (from top to bottom, left to right) of each heat map (F_1-matrix of every regime) in Figure 9 indicating the lowest F_1-scores (yellow and white lines on the heat maps; see also color-bar). The model does not only have the lowest level of agreement with other ensembles but also shows poor accordance within its own members. Generally, the other CMIP6 models exhibit better network similarity during longer regimes (Complete period, AMV+, AMV-, PDV+, PDV-, In-Phase, Out-of-Phase). Members of CESM2 LE strongly agree between each other in terms of causal fingerprints displayed during the analysis on the complete period; this is shown by the dark red box on the second row and second column of the complete period heat map (F_1-matrix). The INM-CM5-0 LE shows low average F_1-scores during the PDV+ and Out-of-Phase regimes, but it surprisingly shows the most agreement between its own ensemble realizations during the complete period, AMV-, PDV- and the In-Phase regimes (see dark red grid boxes in the center of heat maps of these regimes on Figure 9). This implies that the INM-CM5-0 ensemble might involve mostly simulations where PDV and AMV are in the same phase.

The skill of CESM2, CanESM5, MIROC6 and MPI-ESM1-2-LR in recreating the observed causal pathways of the Out-of-Phase regime is also manifested through the better similarity the members of these models show when compared to each other. The heat maps (F_1-matrices in Figure 9) serve to distinguish models with similar causal dynamics. The specified range of internal variability within realizations of the same ensemble (combined with the model-simulated time-varying aerosol forcing) can also be inferred by comparing one LE to itself.

3.4 Discussion

Previous research already suggested the improvement in simulation of dominant modes of climate variability throughout the different phases of the CMIP archive (Fasullo et al., 2020; Eyring et al., 2021). Although, in general, models are able to capture the spatial patterns of these modes, CMIP6 revealed discrepancies in the skill these LE simulations display when recreating the observed modes. Some models perform very well, while there is still room for improvement for others. This conclusion is illustrated through results of the pattern correlations in Sect. 3.1 and the wide range of comparison metrics produced and published by the CVDP-LE authors (Phillips et al., 2020). The ability of CMIP6 LEs to recreate the spatial patterns of modes of climate variability does not, however, ensure that they simulate the connections between those modes. Relative to the reference networks from reanalysis datasets during the Out-of-Phase regime, CESM2, CanESM5, MIROC6 and MPI-ESM1-2-LR LEs display the highest degree of similarity. During the analysis of the complete 1900-2014 period, a considerable fraction of simulations belonging to these CMIP6 models estimates an opposite-sign response from AMV to

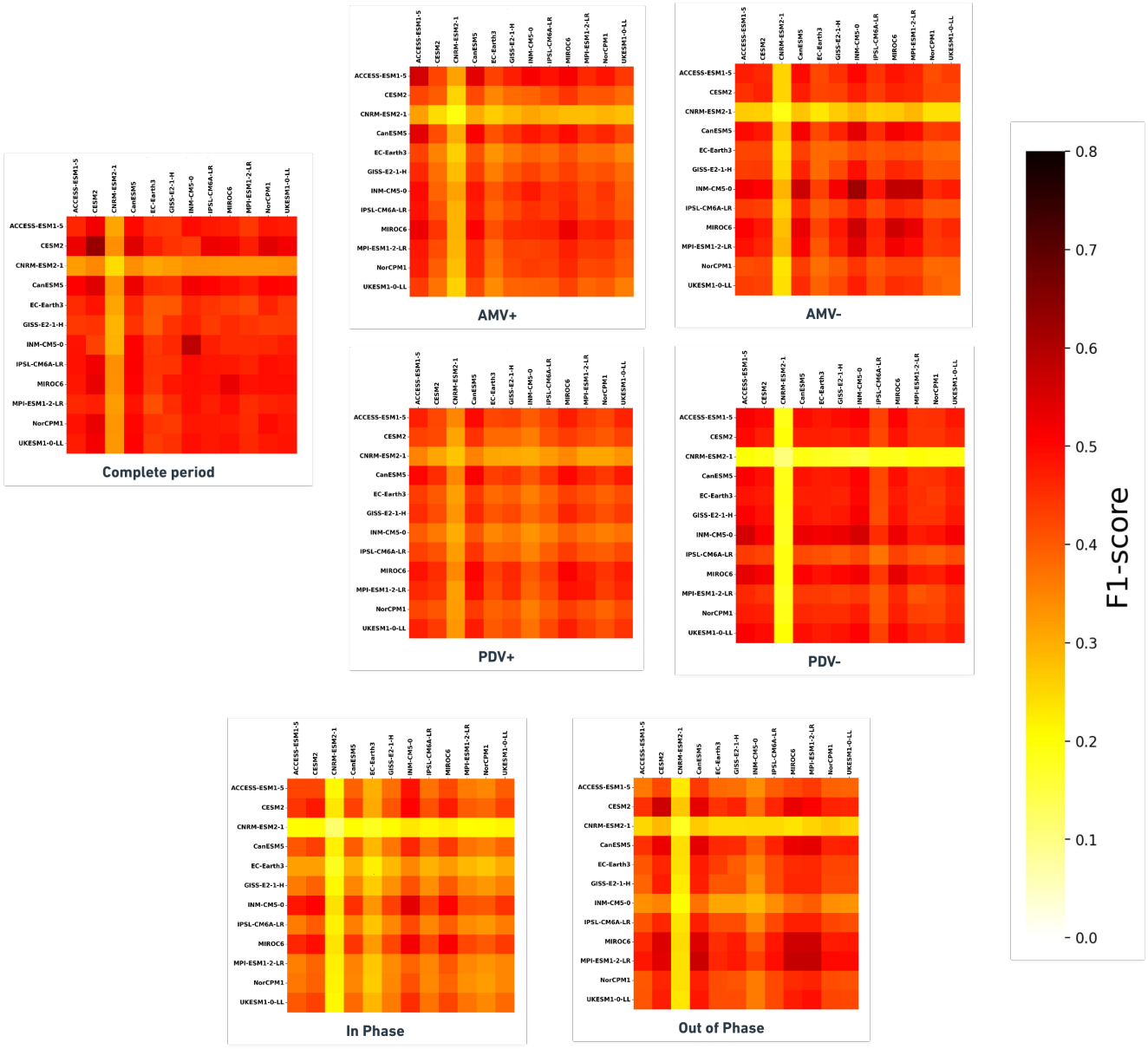

Figure 9. Matrices of average F_1-scores for pair-wise network comparisons between ensemble members of 12 CMIP6 LEs during every regime. Boxes on the main diagonal translate the level of similarity between members of a single CMIP6 ensemble. Boxes outside the main diagonal show the similarity between realizations of a CMIP6 LE compared to realizations from another CMIP6 LE (taking every realization as a reference at a time, before averaging across every LE). The redder the grid box, the better causal network similarity it translates when comparing realizations of the corresponding CMIP6 model (x-axis coordinate name on top of each panel) to causal networks from the corresponding reference CMIP6 model (y-axis coordinate on the left of each panel). The matrices for the short regimes (PDV+/AMV+, PDV+/AMV-, PDV-/AMV+ and PDV-/AMV-) are not shown as their results are not conclusive since PCMCI+ fails to estimate any causal networks for several members of different ensembles.

PDV (represented by blue AMV→PDV links, see Figure A1). The clear occurrence of this opposite-sign response in several CMIP6 LEs (notably, CESM2, CanESM5, MIROC6 and MPI-ESM1-2-LR) shows that these models realistically simulate the mechanisms that connect Atlantic and Pacific modes of SST variability. The direct connection between the Atlantic and Pacific basins involves mainly the tropical Walker circulation and its associated SST, evaporation, wind and SLP changes where rising temperatures in the Atlantic Ocean can cause a cooling effect similar to La Niña in the equatorial Pacific (McGregor et al., 2014; Kucharski et al., 2016; Li et al., 2016; Ruprich-Robert et al., 2021; Meehl et al., 2021a). Moreover, these CMIP6 LEs were found to also simulate most spatial patterns with high correlation coefficients. On the other hand, other LEs such as the UKESM1-0-LL and ACCESS-ESM1-5, despite their high correlation with the observed spatial patterns, do not exhibit the same level of similarity when comparing their causal networks to the reference networks. This discrepancy might be due to the difference in external time-varying aerosol forcing with respect to random internally-generated variability.

In Figure 10 we plot the F_1-scores for all realizations (color- and marker-coded by CMIP6 ensemble, see legend) for the long regimes with respect to the mean-score of r spatial correlations from Sect. 3.1. Similar to Figure 9, we choose not to show the scatter plots for the short regimes. As the mean-scores of spatial correlations are the same for all regimes (computed between the regression maps on the whole 1900-2014 timeseries of the indices), how high (low) a single scatter point can get during a certain regime reveals its causal network similarity (dissimilarity) with reanalysis during that regime. The scatter points closer to the top right corner of each plot belong to realizations which simulate better the spatial patterns and causal fingerprints of reanalysis. Considering only the complete period panel (upper left in Figure 10), the upper right corner of this panel shows mainly realizations from CESM2 (orange crosses), MIROC6 (yellow triangles), CanESM5 (red plus signs) models. From the same panel, we can notice, for example, that the UKESM1-0-LL realizations (orange 5-pointed stars) have great spatial pattern similarity with reanalysis. These UKESM1-0-LL realizations, however, do not show high similarity when comparing their causal fingerprint to that concluded from reanalysis data. The same can be said about MPI-ESM1-2-LR realizations (cyan 6-pointed stars) which, in spite of their high level of skill in recreating the spatial regression patterns of the four modes of climate variability, fail to obtain F_1-scores as high as those from CESM2, CanESM5 or MIROC6 during most regimes. Only during the AMV+ and Out-of-Phase regimes that very few MPI-ESM1-2-LR simulations exceed the 0.7 F_1-score bar. Overall, we can conclude that CESM2 (orange crosses), CanESM5 (red plus signs) and MIROC6 (yellow triangles) undoubtedly outperform other LEs in this evaluation. This is proven through the consistency that simulations from these two LEs show in resembling the observed causal fingerprints during the different regimes. Despite obtaining high spatial correlation coefficients, two members of the IPSL-CM6A-LR model (grey scatters) show the best network similarity with reanalysis during the PDV+ regime while three other members of this model show no similarity during the same regime.

It is worth mentioning that the number of realisations within an LE appears to increase the chance of a model to comprise a simulation with similar dependency structures as those found in observations. The three simulations with the highest F_1-scores during the Out-of-Phase regime (see Figure 8) belong to either CanESM5 or MIROC6 which are the LEs with the highest number of realisations (65 and 50 ensemble members, respectively). This is likely related to the number of realizations needed to capture similar random internal variability to the one observed in reanalysis data. This is less valid for the CESM2 model, which with only 11 realizations, contains simulations with high F_1-scores during most regimes shown in Figure 10. In gen-

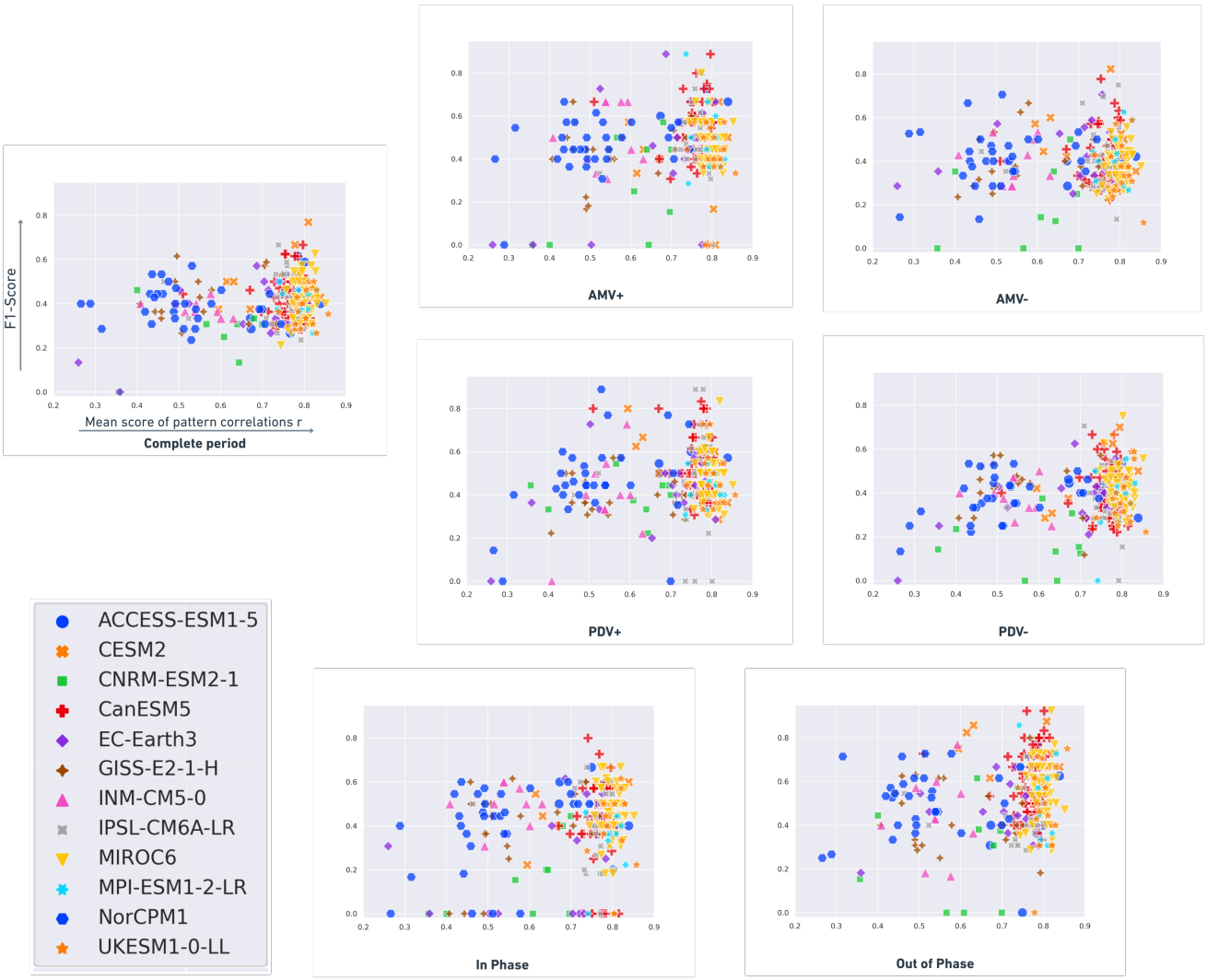

Figure 10. Scatter plots: R_{coef} mean score (spatial correlation with reanalysis, x-axis) vs F_1-score (network similarity with respect to reanalysis, y-axis) during the different regimes. Spatial correlation values do not change from one regime to another; these are the same mean scores calculated from the Pearson r coefficients of the four modes in Sect. 3.1 over the 1900-2014 period. Similar to Figure 9, scatter plots are shown only for the long regimes.

eral, modeling centers previously contributed only a small number of realizations to international climate change projection assessments [e.g., phase 5 of the CMIP (CMIP5; Taylor et al., 2012)]. As a result, model-associated errors and internal climate variability remained difficult, if not impossible, to disentangle (Kay et al., 2015). In this paper, as CMIP6 includes LE models, we overcome this sampling problem by using at least 10 realizations per model (see Table 1). In this way, we have a better estimate of the natural internal variability and the externally forced part. The larger the ensemble size, the more likely that the observed internal variability falls within the plausible internal variability range simulated by that particular LE model realizations. However, despite the improvement of CMIP6 models in capturing the different modes of climate variability (Fasullo et al., 2020), recent studies already pointed to persisting tropical Atlantic biases that knew little or no improvement compared to CMIP5 (Richter and Tokinaga, 2020; Farneti et al., 2022). These biases certainly affect the simulation of Atlantic variability within CMIP6 models as they project additional uncertainties on the AMV-related causal dynamics and spatial patterns. Moreover, previous research showed that, on the decadal timescale, Atlantic mean SST biases in CMIP5 models are directly related to the variability of trade winds over the region (Kajtar et al., 2018). McGregor et al. (2018) found that the addition of the CMIP5 Atlantic bias leads to enhanced descending motion trends in the western and eastern Pacific, and a reduced trend in the central Pacific. The same study found that the observed northward migration of the Intertropical Convergence Zone (ITCZ) is absent when introducing CMIP5 Atlantic bias.

The spatial pattern correlation analysis (Figure 4), the resulting F_1-scores with respect to reanalysis (Figure 8a), and the CMIP6 pair-wise network comparisons (Figure 9) call for the need to investigate the coupling attributes and the simulated internal variability in the CNRM-ESM2-1 ensemble, as its realizations clearly fail to reproduce the observed spatial patterns and causal links between modes of climate variability compared to other CMIP6 LEs. The relatively large distribution of spatial correlation values for the simulated PNA and PDV modes (see purple and red boxes of CNRM-ESM2-1 in Figure 4b), suggest spatial disagreement between the realizations of CNRM-ESM2-1 model regarding the expressed PNA and PDV patterns. This might be the result of a relatively large distribution of forced PNA and/or PDV trends. This can be supported by the timeseries metrics provided by CVDP-LE which reveal that, among the models analysed in this paper (see Table 1), CNRM-ESM2-1 holds the largest 10^{th}-to-90^{th} percentile range of linear PDV trends (-0.89 per 115 years to 1.18 per 115 years) during the 1900-2014 period. These values can be found on the PDV timeseries ensemble summary figure (https://webext.cgd.ucar.edu/Multi-Case/CVDP-LE_repository/CMIP6_Historical_1900-2014/pdv_timeseries_mon.summary.png), as part of the historical 1900-2014 CMIP6 variability diagnostic results distributed by the CVDP-LE authors (Phillips et al., 2020). Considering that the model only counts 10 realizations, the large 10^{th}-to-90^{th} percentile range reveals that the forced PDV trend can be significantly different from one CNRM-ESM2-1 simulation to another. This translates not only to the dissimilarity in terms of spatial PDV patterns within the ensemble members but most probably leads to very different causal dynamics too. The latter can be seen through the causal networks in Appendix Figure A1 and Figure A2 where CNRM-ESM2-1 simulations hardly agree on the sign of the PDV—PNA links (appearing with lighter shades of red) compared to the other CMIP6 models (where PDV—PNA links appear with darker shades of red).

In the present work we defined regimes explicitly based on the phases of PDV and AMV. There are also methods to agnostically extract underlying regimes and their corresponding causal graphs from timeseries (Saggioro et al., 2020), but these are not reliable for the small sample sizes in combination with the high dimensionality of the present datasets.

4 Summary

Applying PCMCI+ to reanalysis data revealed that the direct decadal opposite-sign response from AMV to PDV, described by Meehl et al. (2021a) occurs not only during the analysis of the complete 1900-2014 period (with 11-year time lag), but also during several specified regimes: PDV- (11-year lag), AMV- (11-year lag), PDV+/AMV- (1- and 11-year lags), and when PDV and AMV are out of phase (1- and 11-year lags). These regimes vary from 34-year long (for PDV+/AMV-) to 65-year long (for Out-of-Phase). For the shorter PDV+/AMV+ regime (25-year long) we detect a positive same-sign response from AMV to PDV with a 4-year time delay. The causal networks constructed from the reanalyses datasets have also revealed the same-sign response from PDV to AMV during two regimes: PDV- (59-year long) and PDV-/AMV+ (31-years long). In other words, the regime-oriented causal analysis indicates that AMV might serve as an early predictor of decadal variability over the Pacific. We also find an indirect connection between the Atlantic and Pacific, which is established via PNA during AMV- and PDV+ regimes (both 59-year long), and during PDV-/AMV+. The latter is one of the two regimes that feature a same-sign response from PDV to AMV. An indirect connection between Atlantic and Pacific via the Pacific–South American Pattern is found during the complete 1900-2014 period, where AMV is positively linked with PSA1, but PSA1 has a negative lagged link to PDV. During AMV- regime, the causal graph shows opposite-sign AMV→PSA1→PDV lagged connections.

As an example for the regime-oriented causal analysis on CMIP6 models, we showed the CanESM5 ensemble averaged causal graphs which indicate that the opposite sign effect of AMV on PDV (blue AMV→PDV link) is recreated by several realizations (38 out of 65) during the Out-of-Phase regime, agreeing with the reanalysis results and literature findings (Newman et al., 2016; Johnson et al., 2020). Appendix Figure A1 and Figure A2 show that this opposite sign lagged effect of AMV on PDV was clearly present in simulations belonging to CESM2 and MIROC6 ensembles (AMV→PDV links are clearly blue). The PDV teleconnection to PNA in the form of mutual same-sign response (positive cross-MCI links) was clearly present in most realizations of not only the CanESM5 model (Figure 7) but most of the CMIP6 LE simulations analysed. This is true considering the exception of the CNRM-ESM2-1 simulations which show less agreement between each other on the sign of the PDV—PNA links (appearing with lighter shades of red in Figure A1 and Figure A2) compared to the other CMIP6 models.

The evaluation of the Large Ensembles from the CMIP6 archive presented in this paper unveiled how a model performs compared to other models in terms of simulating observed spatial patterns and causal pathways between modes of climate variability. Most CMIP6 models were found to score better during the Out-of-Phase regime, with CESM2, CanESM5, MIROC6 and MPI-ESM1-2-LR as the best performers during this regime. We showed the importance of using LEs in causal model evaluation to address the sampling issue and explained possible causal pathways during specific regimes that might not appear in causal networks constructed from reanalysis data. Several CanESM5 realizations suggested a same-sign AMV→PDV link during the In-Phase regime. This link did not appear on the In-Phase regime causal graph reconstructed from reanalysis. This

same sign response is nonetheless documented by previous research (Wu et al., 2011; Meehl et al., 2021a). The CanESM5 and MIROC6 models with the highest numbers of members were found to outperform other models in simulating observed causal patterns during the long regimes (see Figure 8a). Interestingly, the CESM2 model, with a relatively smaller ensemble size (11 realizations), was also found to display larger causal fingerprint similarity with reanalysis during the long regimes. The causal network similarity between different CMIP6 LE models was also assessed throughout this paper. Simulations from CESM2, CanESM5 and MIROC6 models also largely resemble each other and those from the MPI-ESM1-2-LR model in terms of estimated causal networks during most regimes (Figure 9).

A deepened intra-model comparison remains essential to evaluate how realizations of the same model ensemble differ from one another. The 'ripf' identifier of every simulation within the CMIP6 LEs used in this study show that some LEs only include realizations (r) with the same initialization (i), physics (p) and forcing (f), while other LEs contain realisations with different physics or forcing. On that account, it is of high importance to inspect the documentation provided by modeling groups on the relevant realization attributes of their model ensemble.

Causal model evaluation is also helping to better understand remote contributions to internal variability over specific regions. As we are not subtracting the ensemble mean (representing the forced response), the causal links found when analysing observational reanalysis and CMIP6 historical simulations are thus expected to include external forcing contributions, especially those from space and time-varying aerosol radiative forcing. It is therefore crucial to separate the internal variability component from the externally forced part to gain a better understanding on the effects of external forcings on Atlantic-Pacific interactions. Meehl et al. (2021a) recently examined this effect through timeseries pacemaker experiments in which effects from aerosols are removed (by fixing aerosols at 1920 values). The approach and findings presented here motivate a follow-up study where pacemaker, pre-industrial control, and future scenario simulations are to be analysed through causal discovery algorithms to reveal the impact of climate change on the teleconnections and interactions between major modes of climate variability. Overall, the regime-oriented causal model evaluation followed in this study has the potential of a powerful methodology that can be applied in a number of environment-related topics, offering tremendous insight to improve the understanding of the complex earth system and the state-of-the-art of climate modeling.

Code and data availability. The complete CVDP-LE diagnostic for the 1900-2014 historical run can be found on the CESM CVCWG CVDP-LE Data Repository, under https://www.cesm.ucar.edu/working_groups/CVC/cvdp-le/data-repository.html. The tigramite package for causal discovery is available under the public Github repository: https://github.com/jakobrunge/tigramite/. The code used to reproduce results and to plot most figures for this paper will be accessible at the time of publication of the manuscript in the following Github repository: https://github.com/EyringMLClimateGroup/karmouche22copernicus_CME_CMIP6.

Appendix A

Table A1. Distribution of Pearson r correlation values between the simulated (CMIP6 LE) and observed (ERA20C_ERA5, ERSSTv5) spatial patterns of PNA, PSA1, PDV, AMV and their Mean Score over the 1900-2014 period. Sorted by Alphabetical order.

CMIP6 LE	Percentile	PNA (DJF)	PSA1 (ANN)	PDV (monthly)	AMV (monthly)	Mean Score
ACCESS-ESM1-5	10th	0.80	0.57	0.68	0.67	0.67
	50th	0.90	0.72	0.71	0.71	0.78
	90th	0.93	0.79	0.77	0.75	0.80
CESM2	10th	0.84	-0.64	0.82	0.68	0.61
	50th	0.88	0.66	0.87	0.73	0.79
	90th	0.91	0.77	0.88	0.77	0.82
CNRM-ESM2-1	10th	0.38	0.39	-0.06	0.73	0.40
	50th	0.59	0.53	0.68	0.74	0.64
	90th	0.84	0.63	0.77	0.79	0.71
CanESM5	10th	0.76	0.56	0.75	0.68	0.73
	50th	0.83	0.75	0.79	0.72	0.77
	90th	0.88	0.81	0.82	0.76	0.80
EC-Earth3	10th	0.81	-0.40	0.45	0.58	0.49
	50th	0.85	0.69	0.71	0.63	0.73
	90th	0.92	0.75	0.77	0.71	0.79
GISS-E2-1-H	10th	0.73	-0.70	0.73	0.62	0.46
	50th	0.79	-0.55	0.77	0.68	0.56
	90th	0.86	0.73	0.81	0.72	0.76
INM-CM5-0	10th	0.53	-0.08	0.47	0.62	0.48
	50th	0.67	0.38	0.50	0.66	0.54
	90th	0.73	0.57	0.56	0.71	0.60
IPSL-CM6A-LR	10th	0.66	0.70	0.75	0.72	0.72
	50th	0.73	0.80	0.79	0.76	0.77
	90th	0.82	0.84	0.81	0.79	0.80
MIROC6	10th	0.81	0.68	0.83	0.67	0.77
	50th	0.86	0.73	0.84	0.71	0.80
	90th	0.91	0.78	0.85	0.74	0.82
MPI-ESM1-2-LR	10th	0.76	0.70	0.75	0.64	0.74
	50th	0.86	0.79	0.80	0.72	0.79
	90th	0.93	0.82	0.83	0.77	0.82
NorCPM1	10th	0.38	-0.58	0.72	0.64	0.41
	50th	0.72	-0.51	0.76	0.68	0.49
	90th	0.82	0.58	0.79	0.72	0.70
UKESM1-0-LL	10th	0.83	0.65	0.80	0.68	0.78
	50th	0.88	0.75	0.82	0.74	0.80
	90th	0.91	0.79	0.86	0.79	0.83

Table A2. Pearson correlation values obtained using 18 UKESM1-0-LL simulation, with respect to the observed (ERA20C_ERA5, ERSSTv5) spatial patterns of PNA, PSA1, PDV, AMV and their Mean Score over the 1900-2014 period. Sorted by mean score.

UKESM1-0-LL Ensemble member	PNA (DJF)	PSA1 (ANN)	PDV (monthly)	AMV (monthly)	**Mean Score**
r19i1p1f2	0.91	0.84	0.86	0.80	0.86
r6i1p1f3	0.89	0.75	0.86	0.78	0.83
r3i1p1f2	0.90	0.76	0.85	0.76	0.83
r14i1p1f2	0.94	0.75	0.82	0.68	0.82
r2i1p1f2	0.88	0.78	0.84	0.75	0.82
r1i1p1f2	0.87	0.81	0.82	0.78	0.82
r11i1p1f2	0.91	0.68	0.81	0.76	0.81
r8i1p1f2	0.90	0.78	0.79	0.70	0.80
r17i1p1f2	0.80	0.76	0.84	0.81	0.80
r7i1p1f3	0.86	0.78	0.82	0.72	0.80
r4i1p1f2	0.90	0.67	0.82	0.73	0.80
r16i1p1f2	0.86	0.75	0.81	0.72	0.79
r10i1p1f2	0.88	0.74	0.83	0.66	0.79
r9i1p1f2	0.89	0.56	0.82	0.77	0.79
r18i1p1f2	0.88	0.60	0.82	0.76	0.78
r5i1p1f3	0.85	0.75	0.81	0.68	0.78
r13i1p1f2	0.84	0.71	0.80	0.74	0.78
r12i1p1f2	0.79	0.67	0.80	0.68	0.74

Table A3. Cross-MCI and auto-MCI values calculated by PCMCI+ from reanalysis timeseries data for the complete 1900-2014 period. Values are relative to the complete period causal graph shown in Figure 2 (right panel) and Figure 5 (upper left panel). The table presents the cross-MCI (cross-correlation) values denoting the sign and strength of the causal link between node *i* and node *j* for lags between 0 and τ_{max}. In bold are the highest absolute cross-MCI values for that specific link (detected within the statistical significance threshold, $\alpha_{pc} \leq 0.05$) and for which links are apparent on the causal graphs. The values are rounded to two decimal places.

	time lag τ	0	1	2	3	4	5	6	7	8	9	10	11	12	13	14	15
i	*j*																
AMV	AMV	0.00	0.45	0.22	0.14	0.17	0.21	0.18	0.18	0.09	0.11	0.05	0.05	0.18	0.09	0.03	0.05
	PNA	0.18	-0.20	-0.06	0.01	-0.13	-0.11	-0.17	-0.04	0.01	-0.04	-0.13	-0.18	-0.17	-0.19	-0.16	-0.06
	PDV	-0.04	-0.18	-0.16	-0.07	-0.12	-0.15	-0.16	-0.18	-0.06	-0.13	-0.21	**-0.25**	0.02	-0.18	-0.06	-0.11
	PSA1	**0.25**	-0.05	-0.01	-0.06	-0.10	-0.11	-0.12	-0.05	-0.06	-0.00	-0.02	-0.07	-0.04	-0.08	-0.00	0.08
PNA	AMV	0.18	-0.05	-0.02	-0.03	-0.09	-0.12	-0.07	0.03	-0.05	0.01	0.01	-0.04	0.05	0.07	0.03	0.03
	PNA	0.00	0.06	0.05	0.04	-0.04	0.10	0.02	0.00	-0.06	-0.11	0.03	-0.14	-0.01	-0.06	-0.11	0.05
	PDV	**0.53**	-0.07	0.10	-0.05	-0.04	0.14	0.16	-0.02	-0.18	-0.10	-0.02	0.01	0.00	-0.07	-0.17	-0.02
	PSA1	0.11	-0.09	0.06	-0.12	-0.08	-0.01	-0.03	-0.05	-0.13	0.00	-0.13	-0.11	0.12	-0.12	-0.10	0.13
PDV	AMV	-0.04	-0.03	-0.01	-0.04	-0.09	-0.15	-0.09	-0.05	0.00	-0.02	0.02	0.02	0.01	0.10	0.12	0.14
	PNA	**0.53**	0.17	0.09	0.04	0.21	0.21	0.05	-0.02	-0.08	-0.08	0.06	0.00	-0.01	-0.02	-0.10	-0.07
	PDV	0.00	0.33	0.18	0.07	0.18	0.18	0.08	0.02	-0.12	-0.01	0.09	0.11	0.02	-0.09	-0.21	-0.15
	PSA1	-0.07	0.11	0.14	0.02	0.03	0.07	0.00	-0.17	-0.13	-0.06	-0.12	-0.09	-0.07	-0.03	-0.09	0.03
PSA1	AMV	**0.25**	-0.09	0.15	-0.09	-0.07	-0.07	-0.06	-0.21	-0.16	-0.14	-0.19	-0.17	-0.16	-0.20	-0.19	-0.15
	PNA	0.11	-0.10	0.18	-0.10	0.04	0.06	0.04	0.21	0.01	0.07	-0.10	0.11	0.11	-0.01	-0.17	-0.09
	PDV	-0.07	0.03	0.11	-0.01	0.02	0.09	0.09	**0.23**	0.08	-0.07	-0.13	-0.07	-0.08	-0.10	-0.21	**-0.31**
	PSA1	0.00	0.04	0.18	0.03	0.19	0.04	0.10	-0.02	-0.16	0.02	-0.09	0.01	-0.09	-0.19	-0.19	0.01

Table A4. Number of years for every regime for: Reanalysis and CMIP6 simulations 1-40.

	Complete Period	AMV+	AMV-	PDV+	PDV-	In-Phase	Out-of-Phase	PDV+/AMV+	PDV+/AMV-	PDV-/AMV+	PDV-/AMV-
Reanalysis	115	56	59	59	56	50	65	25	34	31	25
ACCESS-ESM1-5_r5i1p1f1	115	51	64	60	55	82	33	39	21	12	43
ACCESS-ESM1-5_r1i1p1f1	115	57	58	63	52	71	44	38	25	19	33
ACCESS-ESM1-5_r9i1p1f1	115	57	58	66	49	44	71	26	40	31	18
ACCESS-ESM1-5_r2i1p1f1	115	57	58	63	52	31	84	18	45	39	13
ACCESS-ESM1-5_r8i1p1f1	115	53	62	65	50	59	56	31	34	22	28
ACCESS-ESM1-5_r7i1p1f1	115	64	51	68	47	53	62	35	33	29	18
ACCESS-ESM1-5_r10i1p1f1	115	69	46	58	57	36	79	24	34	45	12
ACCESS-ESM1-5_r4i1p1f1	115	56	59	59	56	42	73	21	38	35	21
ACCESS-ESM1-5_r3i1p1f1	115	68	47	54	61	35	80	21	33	47	14
ACCESS-ESM1-5_r6i1p1f1	115	51	64	48	67	48	67	16	32	35	32
CESM2_r1i1p1f1	115	74	41	61	54	44	71	32	29	42	12
CESM2_r8i1p1f1	115	54	61	54	61	47	68	20	34	34	27
CESM2_r2i1p1f1	115	62	53	42	73	29	86	9	33	53	20
CESM2_r6i1p1f1	115	63	52	67	48	21	94	18	49	45	3
CESM2_r10i1p1f1	115	66	49	50	65	41	74	21	29	45	20
CESM2_r11i1p1f1	115	50	65	54	61	39	76	14	40	36	25
CESM2_r7i1p1f1	115	65	50	51	64	27	88	14	37	51	13
CESM2_r3i1p1f1	115	64	51	58	57	53	62	30	28	34	23
CESM2_r5i1p1f1	115	58	57	56	59	37	78	18	38	40	19
CESM2_r9i1p1f1	115	62	53	57	58	10	105	7	50	55	3
CESM2_r4i1p1f1	115	55	60	65	50	35	80	20	45	35	15
CNRM-ESM2-1_r11i1p1f2	115	44	71	61	54	74	41	32	29	12	42
CNRM-ESM2-1_r4i1p1f2	115	53	62	56	59	28	87	11	45	42	17
CNRM-ESM2-1_r1i1p1f2	115	70	45	59	56	32	83	23	36	47	9
CNRM-ESM2-1_r5i1p1f2	115	54	61	56	59	99	16	47	9	7	52
CNRM-ESM2-1_r7i1p1f2	115	63	52	54	61	70	45	36	18	27	34
CNRM-ESM2-1_r9i1p1f2	115	51	64	65	50	43	72	22	43	29	21
CNRM-ESM2-1_r10i1p1f2	115	54	61	54	61	59	56	26	28	28	33
CNRM-ESM2-1_r3i1p1f2	115	56	59	53	62	82	33	38	15	18	44
CNRM-ESM2-1_r8i1p1f2	115	65	50	76	39	50	65	38	38	27	12
CNRM-ESM2-1_r2i1p1f2	115	54	61	64	51	59	56	31	33	23	28
CanESM5_r15i1p1f1	115	59	56	61	54	45	70	25	36	34	20
CanESM5_r11i1p1f1	115	49	66	66	49	28	87	14	52	35	14
CanESM5_r1i1p2f1	115	60	55	64	51	37	78	23	41	37	14
CanESM5_r19i1p2f1	115	56	59	46	69	39	76	13	33	43	26
CanESM5_r26i1p2f1	115	51	64	63	52	49	66	24	39	27	25
CanESM5_r33i1p2f1	115	62	53	56	59	65	50	34	22	28	31
CanESM5_r31i1p2f1	115	65	50	61	54	61	54	36	25	29	25
CanESM5_r13i1p2f1	115	61	54	55	60	39	76	20	35	41	19
CanESM5_r29i1p2f1	115	55	60	56	59	28	87	12	44	43	16

Table A5. Number of years for every regime for: Reanalysis and CMIP6 simulations 41-80.

	Complete Period	AMV+	AMV-	PDV+	PDV-	In-Phase	Out-of-Phase	PDV+/AMV+	PDV+/AMV-	PDV-/AMV+	PDV-/AMV-
Reanalysis	115	56	59	59	56	50	65	25	34	31	25
CanESM5_r22i1p2f1	115	58	57	55	60	40	75	19	36	39	21
CanESM5_r23i1p1f1	115	47	68	51	64	71	44	27	24	20	44
CanESM5_r6i1p1f1	115	70	45	60	55	33	82	24	36	46	9
CanESM5_r2i1p2f1	115	48	67	48	67	25	90	3	45	45	22
CanESM5_r38i1p2f1	115	65	50	68	47	50	65	34	34	31	16
CanESM5_r19i1p1f1	115	63	52	65	50	37	78	25	40	38	12
CanESM5_r37i1p2f1	115	45	70	63	52	41	74	17	46	28	24
CanESM5_r24i1p1f1	115	59	56	56	59	44	71	22	34	37	22
CanESM5_r4i1p1f1	115	65	50	62	53	40	75	26	36	39	14
CanESM5_r25i1p1f1	115	55	60	57	58	65	50	31	26	24	34
CanESM5_r22i1p1f1	115	61	54	55	60	57	58	29	26	32	28
CanESM5_r12i1p1f1	115	60	55	56	59	63	52	32	24	28	31
CanESM5_r23i1p2f1	115	49	66	64	51	48	67	23	41	26	25
CanESM5_r13i1p1f1	115	53	62	66	49	44	71	24	42	29	20
CanESM5_r4i1p2f1	115	54	61	63	52	50	65	26	37	28	24
CanESM5_r27i1p2f1	115	54	61	55	60	32	83	13	42	41	19
CanESM5_r10i1p2f1	115	61	54	65	50	63	52	37	28	24	26
CanESM5_r16i1p2f1	115	59	56	59	56	47	68	25	34	34	22
CanESM5_r18i1p2f1	115	47	68	49	66	45	70	13	36	34	32
CanESM5_r32i1p2f1	115	59	56	61	54	17	98	11	50	48	6
CanESM5_r17i1p1f1	115	49	66	62	53	28	87	12	50	37	16
CanESM5_r14i1p2f1	115	56	59	52	63	41	74	17	35	39	24
CanESM5_r5i1p1f1	115	51	64	68	47	34	81	19	49	32	15
CanESM5_r24i1p2f1	115	56	59	49	66	50	65	20	29	36	30
CanESM5_r30i1p2f1	115	49	66	58	57	38	77	15	43	34	23
CanESM5_r14i1p1f1	115	54	61	55	60	54	61	24	31	30	30
CanESM5_r21i1p1f1	115	53	62	63	52	27	88	14	49	39	13
CanESM5_r16i1p1f1	115	70	45	56	59	27	88	19	37	51	8
CanESM5_r36i1p2f1	115	51	64	59	56	33	82	14	45	37	19
CanESM5_r3i1p1f1	115	51	64	65	50	49	66	25	40	26	24
CanESM5_r8i1p1f1	115	65	50	51	64	27	88	14	37	51	13
CanESM5_r7i1p2f1	115	43	72	50	65	58	57	18	32	25	40
CanESM5_r6i1p2f1	115	50	65	64	51	67	48	33	31	17	34
CanESM5_r25i1p2f1	115	60	55	43	72	62	53	25	18	35	37
CanESM5_r20i1p1f1	115	54	61	61	54	42	73	21	40	33	21
CanESM5_r5i1p2f1	115	61	54	61	54	35	80	21	40	40	14
CanESM5_r39i1p2f1	115	61	54	51	64	33	82	15	36	46	18
CanESM5_r11i1p2f1	115	52	63	57	58	48	67	21	36	31	27
CanESM5_r2i1p1f1	115	60	55	58	57	25	90	14	44	46	11
CanESM5_r15i1p2f1	115	59	56	62	53	72	43	39	23	20	33

Table A6. Number of years for every regime for: Reanalysis and CMIP6 simulations 81-120.

	Complete Period	AMV+	AMV-	PDV+	PDV-	In-Phase	Out-of-Phase	PDV+/AMV+	PDV+/AMV-	PDV-/AMV+	PDV-/AMV-
Reanalysis	115	56	59	59	56	50	65	25	34	31	25
CanESM5_r9i1p2f1	115	53	62	55	60	49	66	21	34	32	28
CanESM5_r1i1p1f1	115	58	57	60	55	39	76	21	39	37	18
CanESM5_r12i1p2f1	115	59	56	61	54	59	56	32	29	27	27
CanESM5_r18i1p1f1	115	56	59	52	63	57	58	25	27	31	32
CanESM5_r28i1p2f1	115	45	70	51	64	47	68	14	37	31	33
CanESM5_r20i1p2f1	115	55	60	60	55	34	81	17	43	38	17
CanESM5_r10i1p1f1	115	49	66	55	60	59	56	24	31	25	35
CanESM5_r17i1p2f1	115	50	65	56	59	45	70	18	38	32	27
CanESM5_r35i1p2f1	115	57	58	54	61	68	47	32	22	25	36
CanESM5_r3i1p2f1	115	46	69	63	52	62	53	28	35	18	34
CanESM5_r21i1p2f1	115	54	61	56	59	41	74	18	38	36	23
CanESM5_r7i1p1f1	115	58	57	53	62	18	97	7	46	51	11
CanESM5_r8i1p2f1	115	64	51	67	48	36	79	26	41	38	10
CanESM5_r40i1p2f1	115	56	59	63	52	26	89	15	48	41	11
CanESM5_r9i1p1f1	115	42	73	63	52	46	69	18	45	24	28
CanESM5_r34i1p2f1	115	51	64	58	57	20	95	7	51	44	13
EC-Earth3_r22i1p1f1	115	42	73	60	55	45	70	16	44	26	29
EC-Earth3_r6i1p1f1	115	61	54	48	67	28	87	11	37	50	17
EC-Earth3_r23i1p1f1	115	62	53	55	60	30	85	16	39	46	14
EC-Earth3_r3i1p1f1	115	44	71	58	57	33	82	10	48	34	23
EC-Earth3_r17i1p1f1	115	50	65	57	58	46	69	19	38	31	27
EC-Earth3_r19i1p1f1	115	54	61	55	60	56	59	25	30	29	31
EC-Earth3_r12i1p1f1	115	43	72	59	56	47	68	17	42	26	30
EC-Earth3_r20i1p1f1	115	54	61	59	56	46	69	22	37	32	24
EC-Earth3_r10i1p1f1	115	62	53	53	62	20	95	10	43	52	10
EC-Earth3_r18i1p1f1	115	45	70	61	54	21	94	6	55	39	15
EC-Earth3_r24i1p1f1	115	56	59	72	43	43	72	28	44	28	15
EC-Earth3_r9i1p1f1	115	58	57	57	58	46	69	23	34	35	23
EC-Earth3_r1i1p1f1	115	61	54	59	56	47	68	26	33	35	21
EC-Earth3_r14i1p1f1	115	59	56	69	46	103	12	58	11	1	45
EC-Earth3_r16i1p1f1	115	61	54	37	78	27	88	5	32	56	22
EC-Earth3_r7i1p1f1	115	55	60	50	65	30	85	10	40	45	20
EC-Earth3_r4i1p1f1	115	54	61	54	61	37	78	15	39	39	22
EC-Earth3_r21i1p1f1	115	59	56	68	47	64	51	38	30	21	26
EC-Earth3_r2i1p1f1	115	64	51	56	59	51	64	28	28	36	23
EC-Earth3_r25i1p1f1	115	59	56	66	49	82	33	46	20	13	36
GISS-E2-1-H_r2i1p5f1	115	55	60	60	55	46	69	23	37	32	23
GISS-E2-1-H_r1i1p5f1	115	63	52	68	47	42	73	29	39	34	13
GISS-E2-1-H_r1i1p1f2	115	58	57	55	60	50	65	24	31	34	26
GISS-E2-1-H_r8i1p1f1	115	62	53	70	45	73	42	45	25	17	28

Table A7. Number of years for every regime for: Reanalysis and CMIP6 simulations 121-160.

	Complete Period	AMV+	AMV-	PDV+	PDV-	In-Phase	Out-of-Phase	PDV+/AMV+	PDV+/AMV-	PDV-/AMV+	PDV-/AMV-
Reanalysis	115	56	59	59	56	50	65	25	34	31	25
GISS-E2-1-H_r4i1p1f2	115	48	67	61	54	26	89	10	51	38	16
GISS-E2-1-H_r7i1p1f1	115	49	66	53	62	77	38	32	21	17	45
GISS-E2-1-H_r5i1p1f1	115	61	54	53	62	55	60	27	26	34	28
GISS-E2-1-H_r9i1p1f1	115	56	59	67	48	50	65	29	38	27	21
GISS-E2-1-H_r1i1p3f1	115	56	59	63	52	48	67	26	37	30	22
GISS-E2-1-H_r4i1p3f1	115	59	56	66	49	48	67	29	37	30	19
GISS-E2-1-H_r6i1p1f1	115	61	54	57	58	57	58	30	27	31	27
GISS-E2-1-H_r3i1p1f1	115	62	53	56	59	65	50	34	22	28	31
GISS-E2-1-H_r2i1p3f1	115	57	58	58	57	48	67	24	34	33	24
GISS-E2-1-H_r10i1p1f1	115	58	57	51	64	52	63	23	28	35	29
GISS-E2-1-H_r5i1p3f1	115	54	61	54	61	33	82	13	41	41	20
GISS-E2-1-H_r2i1p1f2	115	50	65	53	62	72	43	30	23	20	42
GISS-E2-1-H_r4i1p1f1	115	59	56	63	52	61	54	34	29	25	27
GISS-E2-1-H_r2i1p1f1	115	48	67	64	51	53	62	25	39	23	28
GISS-E2-1-H_r3i1p1f2	115	65	50	50	65	26	89	13	37	52	13
GISS-E2-1-H_r3i1p5f1	115	47	68	55	60	69	46	28	27	19	41
GISS-E2-1-H_r3i1p3f1	115	59	56	61	54	77	38	41	20	18	36
GISS-E2-1-H_r1i1p1f1	115	62	53	51	64	62	53	30	21	32	32
GISS-E2-1-H_r5i1p1f2	115	53	62	61	54	33	82	16	45	37	17
INM-CM5-0_r2i1p1f1	115	60	55	55	60	72	43	36	19	24	36
INM-CM5-0_r6i1p1f1	115	60	55	58	57	63	52	33	25	27	30
INM-CM5-0_r9i1p1f1	115	54	61	57	58	46	69	21	36	33	25
INM-CM5-0_r8i1p1f1	115	60	55	45	70	84	31	37	8	23	47
INM-CM5-0_r4i1p1f1	115	60	55	56	59	53	62	27	29	33	26
INM-CM5-0_r7i1p1f1	115	61	54	59	56	41	74	23	36	38	18
INM-CM5-0_r5i1p1f1	115	60	55	49	66	24	91	9	40	51	15
INM-CM5-0_r1i1p1f1	115	52	63	63	52	56	59	28	35	24	28
INM-CM5-0_r10i1p1f1	115	55	60	55	60	79	36	37	18	18	42
INM-CM5-0_r3i1p1f1	115	60	55	56	59	53	62	27	29	33	26
IPSL-CM6A-LR_r9i1p1f1	115	55	60	54	61	44	71	19	35	36	25
IPSL-CM6A-LR_r15i1p1f1	115	69	46	60	55	30	85	22	38	47	8
IPSL-CM6A-LR_r6i1p1f1	115	71	44	61	54	29	86	23	38	48	6
IPSL-CM6A-LR_r28i1p1f1	115	63	52	65	50	63	52	38	27	25	25
IPSL-CM6A-LR_r31i1p1f1	115	65	50	55	60	45	70	25	30	40	20
IPSL-CM6A-LR_r25i1p1f1	115	51	64	58	57	60	55	27	31	24	33
IPSL-CM6A-LR_r27i1p1f1	115	64	51	58	57	49	66	28	30	36	21
IPSL-CM6A-LR_r30i1p1f1	115	57	58	55	60	51	64	24	31	33	27
IPSL-CM6A-LR_r24i1p1f1	115	59	56	55	60	59	56	29	26	30	30
IPSL-CM6A-LR_r5i1p1f1	115	62	53	60	55	61	54	34	26	28	27
IPSL-CM6A-LR_r22i1p1f1	115	58	57	52	63	79	36	37	15	21	42

Table A8. Number of years for every regime for: Reanalysis and CMIP6 simulations 161-200.

	Complete Period	AMV+	AMV-	PDV+	PDV-	In-Phase	Out-of-Phase	PDV+/AMV+	PDV+/AMV-	PDV-/AMV+	PDV-/AMV-
Reanalysis	115	56	59	59	56	50	65	25	34	31	25
IPSL-CM6A-LR_r26i1p1f1	115	56	59	65	50	48	67	27	38	29	21
IPSL-CM6A-LR_r8i1p1f1	115	57	58	59	56	37	78	19	40	38	18
IPSL-CM6A-LR_r14i1p1f1	115	63	52	54	61	42	73	22	32	41	20
IPSL-CM6A-LR_r10i1p1f1	115	60	55	52	63	45	70	21	31	39	24
IPSL-CM6A-LR_r16i1p1f1	115	54	61	62	53	45	70	23	39	31	22
IPSL-CM6A-LR_r4i1p1f1	115	64	51	56	59	53	62	29	27	35	24
IPSL-CM6A-LR_r20i1p1f1	115	51	64	56	59	62	53	27	29	24	35
IPSL-CM6A-LR_r1i1p1f1	115	56	59	57	58	54	61	26	31	30	28
IPSL-CM6A-LR_r3i1p1f1	115	48	67	52	63	45	70	15	37	33	30
IPSL-CM6A-LR_r7i1p1f1	115	51	64	48	67	44	71	14	34	37	30
IPSL-CM6A-LR_r13i1p1f1	115	65	50	54	61	56	59	30	24	35	26
IPSL-CM6A-LR_r19i1p1f1	115	52	63	56	59	85	30	39	17	13	46
IPSL-CM6A-LR_r23i1p1f1	115	50	65	59	56	36	79	15	44	35	21
IPSL-CM6A-LR_r18i1p1f1	115	53	62	52	63	34	81	12	40	41	22
IPSL-CM6A-LR_r29i1p1f1	115	47	68	56	59	44	71	16	40	31	28
IPSL-CM6A-LR_r2i1p1f1	115	54	61	48	67	35	80	11	37	43	24
IPSL-CM6A-LR_r11i1p1f1	115	56	59	61	54	52	63	27	34	29	25
IPSL-CM6A-LR_r32i1p1f1	115	53	62	62	53	54	61	27	35	26	27
IPSL-CM6A-LR_r21i1p1f1	115	63	52	59	56	35	80	21	38	42	14
IPSL-CM6A-LR_r17i1p1f1	115	50	65	60	55	39	76	17	43	33	22
IPSL-CM6A-LR_r12i1p1f1	115	57	58	54	61	66	49	31	23	26	35
MIROC6_r35i1p1f1	115	46	69	55	60	38	77	12	43	34	26
MIROC6_r32i1p1f1	115	64	51	55	60	46	69	25	30	39	21
MIROC6_r40i1p1f1	115	58	57	56	59	47	68	23	33	35	24
MIROC6_r20i1p1f1	115	60	55	60	55	41	74	23	37	37	18
MIROC6_r11i1p1f1	115	58	57	58	57	33	82	17	41	41	16
MIROC6_r44i1p1f1	115	66	49	59	56	54	61	32	27	34	22
MIROC6_r4i1p1f1	115	46	69	57	58	42	73	15	42	31	27
MIROC6_r13i1p1f1	115	59	56	67	48	39	76	25	42	34	14
MIROC6_r3i1p1f1	115	51	64	62	53	56	59	27	35	24	29
MIROC6_r46i1p1f1	115	63	52	49	66	47	68	22	27	41	25
MIROC6_r9i1p1f1	115	60	55	57	58	42	73	22	35	38	20
MIROC6_r14i1p1f1	115	58	57	61	54	58	57	31	30	27	27
MIROC6_r15i1p1f1	115	42	73	60	55	41	74	14	46	28	27
MIROC6_r21i1p1f1	115	59	56	63	52	49	66	28	35	31	21
MIROC6_r38i1p1f1	115	59	56	57	58	25	90	13	44	46	12
MIROC6_r31i1p1f1	115	57	58	58	57	62	53	31	27	26	31
MIROC6_r16i1p1f1	115	64	51	73	42	50	65	36	37	28	14
MIROC6_r29i1p1f1	115	63	52	65	50	55	60	34	31	29	21
MIROC6_r2i1p1f1	115	44	71	48	67	51	64	14	34	30	37

Table A9. Number of years for every regime for: Reanalysis and CMIP6 simulations 201-240.

	Complete Period	AMV+	AMV-	PDV+	PDV-	In-Phase	Out-of-Phase	PDV+/AMV+	PDV+/AMV-	PDV-/AMV+	PDV-/AMV-
Reanalysis	115	56	59	59	56	50	65	25	34	31	25
MIROC6_r34i1p1f1	115	61	54	47	68	69	46	31	16	30	38
MIROC6_r1i1p1f1	115	70	45	53	62	52	63	30	23	40	22
MIROC6_r39i1p1f1	115	64	51	54	61	57	58	30	24	34	27
MIROC6_r8i1p1f1	115	52	63	61	54	68	47	33	28	19	35
MIROC6_r42i1p1f1	115	57	58	57	58	59	56	29	28	28	30
MIROC6_r27i1p1f1	115	74	41	60	55	73	42	46	14	28	27
MIROC6_r26i1p1f1	115	66	49	55	60	42	73	24	31	42	18
MIROC6_r17i1p1f1	115	55	60	59	56	49	66	24	35	31	25
MIROC6_r48i1p1f1	115	56	59	66	49	69	46	38	28	18	31
MIROC6_r6i1p1f1	115	53	62	57	58	45	70	20	37	33	25
MIROC6_r30i1p1f1	115	57	58	53	62	53	62	24	29	33	29
MIROC6_r49i1p1f1	115	54	61	63	52	52	63	27	36	27	25
MIROC6_r5i1p1f1	115	58	57	68	47	57	58	34	34	24	23
MIROC6_r41i1p1f1	115	64	51	57	58	46	69	26	31	38	20
MIROC6_r23i1p1f1	115	56	59	55	60	46	69	21	34	35	25
MIROC6_r12i1p1f1	115	54	61	55	60	42	73	18	37	36	24
MIROC6_r10i1p1f1	115	57	58	67	48	37	78	23	44	34	14
MIROC6_r24i1p1f1	115	62	53	56	59	51	64	27	29	35	24
MIROC6_r33i1p1f1	115	55	60	66	49	38	77	22	44	33	16
MIROC6_r7i1p1f1	115	57	58	58	57	26	89	13	45	44	13
MIROC6_r36i1p1f1	115	74	41	59	56	42	73	30	29	44	12
MIROC6_r28i1p1f1	115	57	58	56	59	46	69	22	34	35	24
MIROC6_r37i1p1f1	115	62	53	62	53	63	52	36	26	26	27
MIROC6_r47i1p1f1	115	61	54	48	67	44	71	19	29	42	25
MIROC6_r19i1p1f1	115	50	65	59	56	62	53	28	31	22	34
MIROC6_r18i1p1f1	115	56	59	55	60	48	67	22	33	34	26
MIROC6_r22i1p1f1	115	65	50	49	66	35	80	17	32	48	18
MIROC6_r43i1p1f1	115	67	48	57	58	31	84	20	37	47	11
MIROC6_r50i1p1f1	115	58	57	47	68	26	89	8	39	50	18
MIROC6_r25i1p1f1	115	57	58	55	60	49	66	23	32	34	26
MIROC6_r45i1p1f1	115	70	45	59	56	32	83	23	36	47	9
MPI-ESM1-2-LR_r2i1p1f1	115	62	53	55	60	66	49	34	21	28	32
MPI-ESM1-2-LR_r10i1p1f1	115	54	61	50	65	51	64	20	30	34	31
MPI-ESM1-2-LR_r3i1p1f1	115	59	56	64	51	58	57	33	31	26	25
MPI-ESM1-2-LR_r5i1p1f1	115	64	51	61	54	42	73	26	35	38	16
MPI-ESM1-2-LR_r8i1p1f1	115	59	56	51	64	57	58	26	25	33	31
MPI-ESM1-2-LR_r7i1p1f1	115	50	65	68	47	23	92	13	55	37	10
MPI-ESM1-2-LR_r9i1p1f1	115	60	55	58	57	65	50	34	24	26	31
MPI-ESM1-2-LR_r4i1p1f1	115	64	51	55	60	48	67	26	29	38	22
MPI-ESM1-2-LR_r6i1p1f1	115	52	63	61	54	58	57	28	33	24	30

Table A10. Number of years for every regime for: Reanalysis and CMIP6 simulations 241-289.

	Complete Period	AMV+	AMV-	PDV+	PDV-	In-Phase	Out-of-Phase	PDV+/AMV+	PDV+/AMV-	PDV-/AMV+	PDV-/AMV-
Reanalysis	115	56	59	59	56	50	65	25	34	31	25
MPI-ESM1-2-LR_r1i1p1f1	115	64	51	66	49	57	58	36	30	28	21
NorCPM1_r20i1p1f1	115	58	57	49	66	48	67	20	29	38	28
NorCPM1_r19i1p1f1	115	54	61	58	57	27	88	12	46	42	15
NorCPM1_r13i1p1f1	115	53	62	51	64	31	84	10	41	43	21
NorCPM1_r29i1p1f1	115	56	59	53	62	52	63	23	30	33	29
NorCPM1_r4i1p1f1	115	53	62	44	71	48	67	15	29	38	33
NorCPM1_r18i1p1f1	115	59	56	58	57	40	75	21	37	38	19
NorCPM1_r30i1p1f1	115	63	52	52	63	62	53	31	21	32	31
NorCPM1_r27i1p1f1	115	52	63	65	50	44	71	23	42	29	21
NorCPM1_r2i1p1f1	115	56	59	61	54	34	81	18	43	38	16
NorCPM1_r5i1p1f1	115	57	58	47	68	55	60	22	25	35	33
NorCPM1_r22i1p1f1	115	59	56	47	68	37	78	14	33	45	23
NorCPM1_r3i1p1f1	115	56	59	65	50	48	67	27	38	29	21
NorCPM1_r16i1p1f1	115	44	71	59	56	26	89	7	52	37	19
NorCPM1_r17i1p1f1	115	66	49	48	67	35	80	17	31	49	18
NorCPM1_r9i1p1f1	115	60	55	56	59	33	82	17	39	43	16
NorCPM1_r8i1p1f1	115	46	69	52	63	55	60	19	33	27	36
NorCPM1_r11i1p1f1	115	50	65	43	72	54	61	16	27	34	38
NorCPM1_r6i1p1f1	115	65	50	64	51	54	61	34	30	31	20
NorCPM1_r23i1p1f1	115	55	60	65	50	29	86	17	48	38	12
NorCPM1_r1i1p1f1	115	57	58	70	45	44	71	28	42	29	16
NorCPM1_r14i1p1f1	115	61	54	55	60	63	52	32	23	29	31
NorCPM1_r21i1p1f1	115	54	61	50	65	33	82	11	39	43	22
NorCPM1_r7i1p1f1	115	59	56	57	58	55	60	28	29	31	27
NorCPM1_r10i1p1f1	115	64	51	56	59	87	28	46	10	18	41
NorCPM1_r26i1p1f1	115	54	61	47	68	40	75	13	34	41	27
NorCPM1_r25i1p1f1	115	65	50	63	52	67	48	40	23	25	27
NorCPM1_r12i1p1f1	115	60	55	53	62	54	61	26	27	34	28
NorCPM1_r24i1p1f1	115	58	57	56	59	43	72	21	35	37	22
NorCPM1_r28i1p1f1	115	66	49	50	65	31	84	16	34	50	15
NorCPM1_r15i1p1f1	115	67	48	45	70	65	50	31	14	36	34
UKESM1-0-LL_r16i1p1f2	115	62	53	67	48	70	45	42	25	20	28
UKESM1-0-LL_r3i1p1f2	115	63	52	58	57	54	61	30	28	33	24
UKESM1-0-LL_r8i1p1f2	115	46	69	59	56	44	71	17	42	29	27
UKESM1-0-LL_r14i1p1f2	115	57	58	59	56	73	42	37	22	20	36
UKESM1-0-LL_r13i1p1f2	115	49	66	52	63	80	35	33	19	16	47
UKESM1-0-LL_r11i1p1f2	115	71	44	56	59	12	103	12	44	59	0
UKESM1-0-LL_r12i1p1f2	115	68	47	69	46	26	89	24	45	44	2
UKESM1-0-LL_r9i1p1f2	115	59	56	54	61	46	69	22	32	37	24
UKESM1-0-LL_r7i1p1f3	115	60	55	74	41	37	78	28	46	32	9
UKESM1-0-LL_r17i1p1f2	115	50	65	68	47	35	80	19	49	31	16
UKESM1-0-LL_r1i1p1f2	115	62	53	51	64	44	71	21	30	41	23
UKESM1-0-LL_r5i1p1f3	115	65	50	50	65	72	43	36	14	29	36
UKESM1-0-LL_r2i1p1f2	115	45	70	49	66	47	68	13	36	32	34
UKESM1-0-LL_r10i1p1f2	115	47	68	51	64	47	68	15	36	32	32
UKESM1-0-LL_r19i1p1f2	115	73	42	57	58	39	76	27	30	46	12
UKESM1-0-LL_r18i1p1f2	115	48	67	66	49	41	74	20	46	28	21
UKESM1-0-LL_r6i1p1f3	115	70	45	60	55	47	68	31	29	39	16
UKESM1-0-LL_r4i1p1f2	115	56	59	63	52	52	63	28	35	28	24

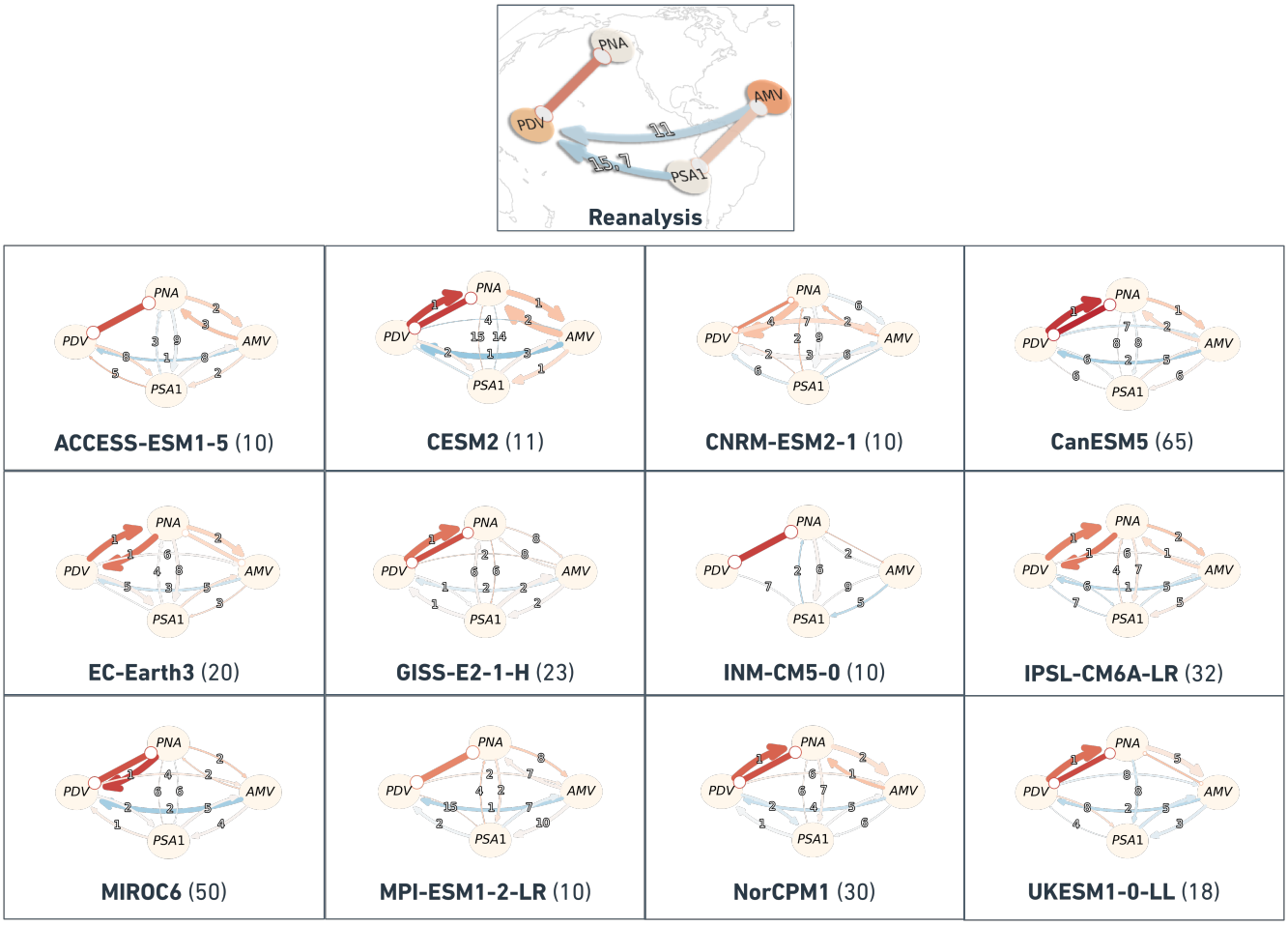

Figure A1. Similar to Figure 7 but for the 12 CMIP6 models during the *complete 1900-2014 period*. Each panel has a label stating the model name and the number of ensemble members between parenthesis. The auto-MCI values were not taken into consideration.

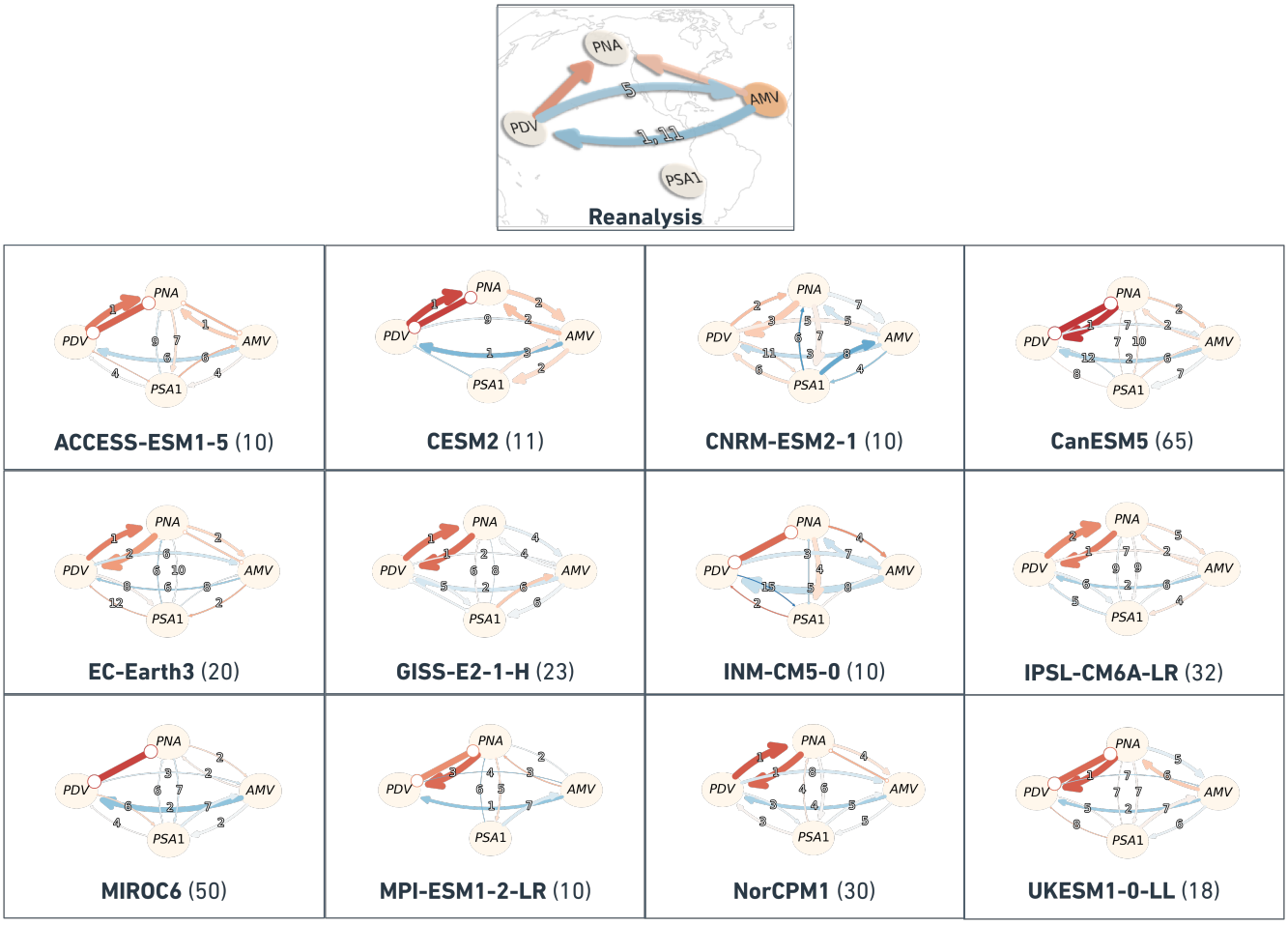

Figure A2. Similar to Figure 7 but for the 12 CMIP6 models during the *Out-of-Phase regime*. Each panel has a label stating the model name and the number of ensemble members between parenthesis. The auto-MCI values were not taken into consideration.

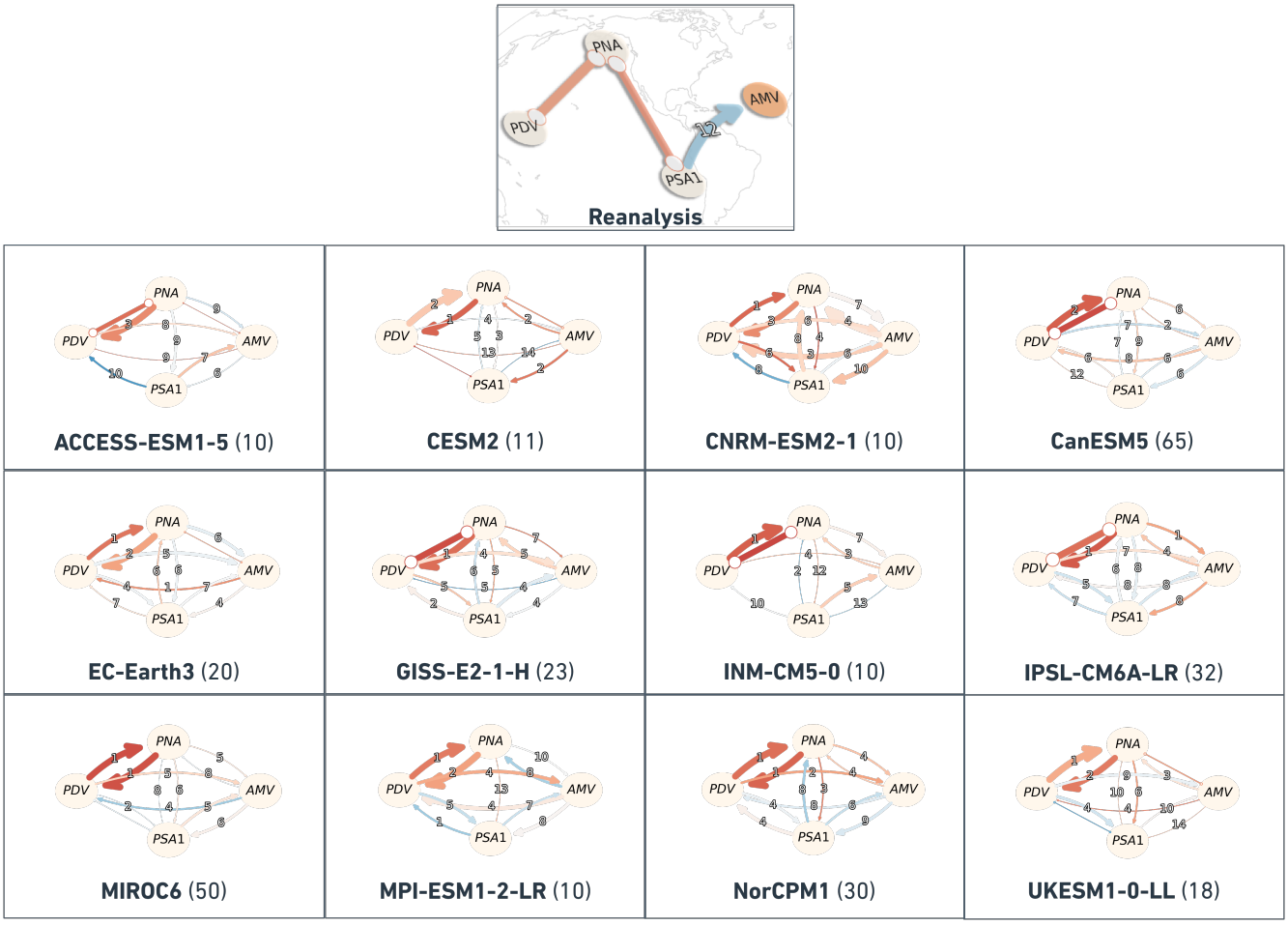

Figure A3. Similar to Figure 7 but for the 12 CMIP6 models during the *In-Phase regime*. Each panel has a label stating the model name and the number of ensemble members between parenthesis. The auto-MCI values were not taken into consideration.

Author contributions. SK and VE designed and organized the study and lead the interpretation of the results. SK lead the writing of the manuscript, performed the data processing and analysis, and prepared all figures and tables. EG contributed to the concept of the study and supported the analysis. JR developed a new version of the causal discovery tool that supported this study. JM, AP, and KW contributed to the interpretation of the results. All coauthors contributed to the writing of the manuscript.

Competing interests. The authors declare that they have no conflict of interest.

Acknowledgements. Funding for this study was provided by the European Research Council (ERC) Synergy Grant "Understanding and modeling the Earth System with Machine Learning (USMILE)" under the Horizon 2020 research and innovation program (Grant agreement No. 855187) and the "Advanced Earth System Model Evaluation for CMIP (EVal4CMIP)" project funded by the Helmholtz Society. We acknowledge the World Climate Research Program's (WCRP's) Working Group on Coupled Modelling (WGCM), which is responsible for CMIP, and we thank the climate modelling groups listed in Table 1 for producing and making available their model output. This work used resources of the Deutsches Klimarechenzentrum (DKRZ) granted by its Scientific Steering Committee (WLA) under project ID bd1083.

References

Arblaster, J., Meehl, G., and Moore, A.: Interdecadal modulation of Australian rainfall, Climate Dynamics, 18, 519–531, 2002.

Bethke, I., Wang, Y., Counillon, F., Kimmritz, M., Fransner, F., Samuelsen, A., Langehaug, H. R., Chiu, P.-G., Bentsen, M., Guo, C., Tjiputra, J., Kirkevåg, A., Oliviè, D. J. L., Seland, y., Fan, Y., Lawrence, P., Eldevik, T., and Keenlyside, N.: NCC NorCPM1 model output prepared for CMIP6 CMIP, https://doi.org/10.22033/ESGF/CMIP6.10843, 2019.

Booth, B. B., Dunstone, N. J., Halloran, P. R., Andrews, T., and Bellouin, N.: Aerosols implicated as a prime driver of twentieth-century North Atlantic climate variability, Nature, 484, 228–232, 2012.

Boucher, O., Denvil, S., Levavasseur, G., Cozic, A., Caubel, A., Foujols, M.-A., Meurdesoif, Y., Cadule, P., Devilliers, M., Ghattas, J., Lebas, N., Lurton, T., Mellul, L., Musat, I., Mignot, J., and Cheruy, F.: IPSL IPSL-CM6A-LR model output prepared for CMIP6 CMIP, https://doi.org/10.22033/ESGF/CMIP6.1534, 2018.

Chen, X. and Wallace, J. M.: ENSO-like variability: 1900–2013, Journal of Climate, 28, 9623–9641, 2015.

Chikamoto, Y., Timmermann, A., Luo, J.-J., Mochizuki, T., Kimoto, M., Watanabe, M., Ishii, M., Xie, S.-P., and Jin, F.-F.: Skilful multi-year predictions of tropical trans-basin climate variability, Nature communications, 6, 1–7, 2015.

Chylek, P., Dubey, M. K., Lesins, G., Li, J., and Hengartner, N.: Imprint of the Atlantic multi-decadal oscillation and Pacific decadal oscillation on southwestern US climate: Past, present, and future, Climate dynamics, 43, 119–129, 2014.

Danabasoglu, G.: NCAR CESM2 model output prepared for CMIP6 CMIP historical, https://doi.org/10.22033/ESGF/CMIP6.7627, 2019.

Deser, C., Phillips, A. S., Bourdette, V., and Teng, H.: Uncertainty in climate change projections: the role of internal variability, Climate dynamics, 38, 527–546, 2012.

Dong, L., Zhou, T., and Chen, X.: Changes of Pacific decadal variability in the twentieth century driven by internal variability, greenhouse gases, and aerosols, Geophysical Research Letters, 41, 8570–8577, 2014.

d'Orgeville, M. and Peltier, W. R.: On the Pacific decadal oscillation and the Atlantic multidecadal oscillation: might they be related?, Geophysical Research Letters, 34, 2007.

Döscher, R., Acosta, M., Alessandri, A., Anthoni, P., Arsouze, T., Bergman, T., Bernardello, R., Boussetta, S., Caron, L.-P., Carver, G., Castrillo, M., Catalano, F., Cvijanovic, I., Davini, P., Dekker, E., Doblas-Reyes, F. J., Docquier, D., Echevarria, P., Fladrich, U., Fuentes-Franco, R., Gröger, M., v. Hardenberg, J., Hieronymus, J., Karami, M. P., Keskinen, J.-P., Koenigk, T., Makkonen, R., Massonnet, F., Ménégoz, M., Miller, P. A., Moreno-Chamarro, E., Nieradzik, L., van Noije, T., Nolan, P., O'Donnell, D., Ollinaho, P., van den Oord, G., Ortega, P., Prims, O. T., Ramos, A., Reerink, T., Rousset, C., Ruprich-Robert, Y., Le Sager, P., Schmith, T., Schrödner, R., Serva, F., Sicardi, V., Sloth Madsen, M., Smith, B., Tian, T., Tourigny, E., Uotila, P., Vancoppenolle, M., Wang, S., Wårlind, D., Willén, U., Wyser, K., Yang, S., Yepes-Arbós, X., and Zhang, Q.: The EC-Earth3 Earth system model for the Coupled Model Intercomparison Project 6, Geoscientific Model Development, 15, 2973–3020, https://doi.org/10.5194/gmd-15-2973-2022, 2022.

Ebbesmeyer, C. C., Cayan, D. R., McLain, D. R., Nichols, F. H., Peterson, D. H., and Redmond, K. T.: 1976 step in the Pacific climate: forty environmental changes between 1968-1975 and 1977-1984, 1991.

Ebert-Uphoff, I. and Deng, Y.: Causal discovery for climate research using graphical models, Journal of Climate, 25, 5648–5665, 2012.

Eyring, V., Bony, S., Meehl, G. A., Senior, C. A., Stevens, B., Stouffer, R. J., and Taylor, K. E.: Overview of the Coupled Model Intercomparison Project Phase 6 (CMIP6) experimental design and organization, Geoscientific Model Development, 9, 1937–1958, 2016.

Eyring, V., Cox, P. M., Flato, G. M., Gleckler, P. J., Abramowitz, G., Caldwell, P., Collins, W. D., Gier, B. K., Hall, A. D., Hoffman, F. M., et al.: Taking climate model evaluation to the next level, Nature Climate Change, 9, 102–110, 2019.

Eyring, V., Gillett, N., Achutarao, K., Barimalala, R., Barreiro Parrillo, M., Bellouin, N., Cassou, C., Durack, P., Kosaka, Y., McGregor, S., et al.: Human Influence on the Climate System: Contribution of Working Group I to the Sixth Assessment Report of the Intergovernmental Panel on Climate Change, IPCC Sixth Assessment Report, 2021.

Fang, C., Wu, L., and Zhang, X.: The impact of global warming on the Pacific Decadal Oscillation and the possible mechanism, Advances in Atmospheric Sciences, 31, 118–130, 2014.

Farneti, R., Stiz, A., and Ssebandeke, J. B.: Improvements and persistent biases in the southeast tropical Atlantic in CMIP models, npj Climate and Atmospheric Science, 5, 1–11, 2022.

Fasullo, J. T., Phillips, A. S., and Deser, C.: Evaluation of leading modes of climate variability in the CMIP archives, Journal of Climate, 33, 5527–5545, 2020.

Folland, C. K., Palmer, T. N., and Parker, D. E.: Sahel rainfall and worldwide sea temperatures, 1901–85, Nature, 320, 602–607, 1986.

Fyfe, J. C., Meehl, G. A., England, M. H., Mann, M. E., Santer, B. D., Flato, G. M., Hawkins, E., Gillett, N. P., Xie, S.-P., Kosaka, Y., et al.: Making sense of the early-2000s warming slowdown, Nature Climate Change, 6, 224–228, 2016.

Gerhardus, A. and Runge, J.: High-recall causal discovery for autocorrelated time series with latent confounders, Advances in Neural Information Processing Systems, 33, 12 615–12 625, 2020.

Huang, B., Thorne, P. W., Banzon, V. F., Boyer, T., Chepurin, G., Lawrimore, J. H., Menne, M. J., Smith, T. M., Vose, R. S., and Zhang, H.-M.: Extended reconstructed sea surface temperature, version 5 (ERSSTv5): upgrades, validations, and intercomparisons, Journal of Climate, 30, 8179–8205, 2017.

IPCC: AR6, Annex IV: Modes of Variability [Cassou, C., A. Cherchi, Y. Kosaka (eds.)]. In *Climate Change 2021: The Physical Science Basis. Contribution of Working Group I to the Sixth Assessment Report of the Intergovernmental Panel on Climate Change* [Masson-Delmotte, V., P. Zhai, A. Pirani, S.L. Connors, C. Péan, S. Berger, N. Caud, Y. Chen, L. Goldfarb, M.I. Gomis, M. Huang, K. Leitzell, E. Lonnoy, J.B.R. Matthews, T.K. Maycock, T. Waterfield, O. Yelekçi, R. Yu, and B. Zhou (eds.)]. Cambridge, United Kingdom and New York, NY, USA, pp. 2153–2192, doi:10.1017/9781009157896.018, 2021.

Johnson, N. C., Amaya, D. J., Ding, Q., Kosaka, Y., Tokinaga, H., and Xie, S.-P.: Multidecadal modulations of key metrics of global climate change, Global and Planetary Change, 188, 103 149, 2020.

Kajtar, J. B., Santoso, A., McGregor, S., England, M. H., and Baillie, Z.: Model under-representation of decadal Pacific trade wind trends and its link to tropical Atlantic bias, Climate dynamics, 50, 1471–1484, 2018.

Kay, J. E., Deser, C., Phillips, A. S., Mai, A., Hannay, C., Strand, G., Arblaster, J. M., Bates, S., Danabasoglu, G., Edwards, J., et al.: The Community Earth System Model (CESM) large ensemble project: A community resource for studying climate change in the presence of internal climate variability, Bulletin of the American Meteorological Society, 96, 1333–1349, 2015.

Kelley, M., Schmidt, G. A., Nazarenko, L. S., Bauer, S. E., Ruedy, R., Russell, G. L., Ackerman, A. S., Aleinov, I., Bauer, M., Bleck, R., et al.: GISS-E2. 1: Configurations and climatology, Journal of Advances in Modeling Earth Systems, 12, e2019MS002 025, 2020.

Kerr, R. A.: A North Atlantic climate pacemaker for the centuries, Science, 288, 1984–1985, 2000.

Knight, J. R., Folland, C. K., and Scaife, A. A.: Climate impacts of the Atlantic multidecadal oscillation, Geophysical Research Letters, 33, 2006.

Kucharski, F., Ikram, F., Molteni, F., Farneti, R., Kang, I.-S., No, H.-H., King, M. P., Giuliani, G., and Mogensen, K.: Atlantic forcing of Pacific decadal variability, Climate Dynamics, 46, 2337–2351, 2016.

Li, X., Xie, S.-P., Gille, S. T., and Yoo, C.: Atlantic-induced pan-tropical climate change over the past three decades, Nature Climate Change, 6, 275–279, 2016.

Maher, N., McGregor, S., England, M. H., and Gupta, A. S.: Effects of volcanism on tropical variability, Geophysical Research Letters, 42, 6024–6033, 2015.

Mantua, N. J., Hare, S. R., Zhang, Y., Wallace, J. M., and Francis, R. C.: A Pacific interdecadal climate oscillation with impacts on salmon production, Bulletin of the american Meteorological Society, 78, 1069–1080, 1997.

McGregor, S., Timmermann, A., Stuecker, M. F., England, M. H., Merrifield, M., Jin, F.-F., and Chikamoto, Y.: Recent Walker circulation strengthening and Pacific cooling amplified by Atlantic warming, Nature Climate Change, 4, 888–892, 2014.

McGregor, S., Stuecker, M. F., Kajtar, J. B., England, M. H., and Collins, M.: Model tropical Atlantic biases underpin diminished Pacific decadal variability, Nature Climate Change, 8, 493–498, 2018.

Meehl, G. A., Hu, A., and Santer, B. D.: The mid-1970s climate shift in the Pacific and the relative roles of forced versus inherent decadal variability, Journal of Climate, 22, 780–792, 2009.

Meehl, G. A., Hu, A., Arblaster, J. M., Fasullo, J., and Trenberth, K. E.: Externally forced and internally generated decadal climate variability associated with the Interdecadal Pacific Oscillation, Journal of Climate, 26, 7298–7310, 2013.

Meehl, G. A., Hu, A., Santer, B. D., and Xie, S.-P.: Contribution of the Interdecadal Pacific Oscillation to twentieth-century global surface temperature trends, Nature Climate Change, 6, 1005–1008, 2016.

Meehl, G. A., Hu, A., Castruccio, F., England, M. H., Bates, S. C., Danabasoglu, G., McGregor, S., Arblaster, J. M., Xie, S.-P., and Rosenbloom, N.: Atlantic and Pacific tropics connected by mutually interactive decadal-timescale processes, Nature Geoscience, 14, 36–42, 2021a.

Meehl, G. A., Teng, H., Capotondi, A., and Hu, A.: The role of interannual ENSO events in decadal timescale transitions of the Interdecadal Pacific Oscillation, Climate Dynamics, 57, 1933–1951, 2021b.

Mo, K. C. and Higgins, R. W.: The Pacific–South American modes and tropical convection during the Southern Hemisphere winter, Monthly Weather Review, 126, 1581–1596, 1998.

Newman, M., Alexander, M. A., Ault, T. R., Cobb, K. M., Deser, C., Di Lorenzo, E., Mantua, N. J., Miller, A. J., Minobe, S., Nakamura, H., et al.: The Pacific decadal oscillation, revisited, Journal of Climate, 29, 4399–4427, 2016.

Nigam, S., Sengupta, A., and Ruiz-Barradas, A.: Atlantic–Pacific links in observed multidecadal SST variability: is the Atlantic multidecadal oscillation's phase reversal orchestrated by the Pacific decadal oscillation?, Journal of Climate, 33, 5479–5505, 2020.

Nitta, T. and Yamada, S.: Recent warming of tropical sea surface temperature and its relationship to the Northern Hemisphere circulation, Journal of the Meteorological Society of Japan. Ser. II, 67, 375–383, 1989.

Nowack, P., Runge, J., Eyring, V., and Haigh, J. D.: Causal networks for climate model evaluation and constrained projections, Nature communications, 11, 1–11, 2020.

Phillips, A. S., Deser, C., and Fasullo, J.: Evaluating modes of variability in climate models, Eos, Transactions American Geophysical Union, 95, 453–455, 2014.

Phillips, A. S., Deser, C., Fasullo, J., Schneider, D., and Simpson, I.: Assessing Climate Variability and Change in Model Large Ensembles: A User's Guide to the "Climate Variability Diagnostics Package for Large Ensembles", version 1, version, 1, 0, 2020.

Power, S., Casey, T., Folland, C., Colman, A., and Mehta, V.: Inter-decadal modulation of the impact of ENSO on Australia, Climate Dynamics, 15, 319–324, 1999.

Richter, I. and Tokinaga, H.: An overview of the performance of CMIP6 models in the tropical Atlantic: mean state, variability, and remote impacts, Climate Dynamics, 55, 2579–2601, 2020.

Runge, J.: Causal network reconstruction from time series: From theoretical assumptions to practical estimation, Chaos: An Interdisciplinary Journal of Nonlinear Science, 28, 075 310, 2018.

Runge, J.: Discovering contemporaneous and lagged causal relations in autocorrelated nonlinear time series datasets, in: Conference on Uncertainty in Artificial Intelligence, pp. 1388–1397, PMLR, 2020.

Runge, J.: Necessary and sufficient graphical conditions for optimal adjustment sets in causal graphical models with hidden variables, Advances in Neural Information Processing Systems, 34, 15 762–15 773, 2021.

Runge, J., Petoukhov, V., Donges, J. F., Hlinka, J., Jajcay, N., Vejmelka, M., Hartman, D., Marwan, N., Paluš, M., and Kurths, J.: Identifying causal gateways and mediators in complex spatio-temporal systems, Nature communications, 6, 1–10, 2015.

Runge, J., Bathiany, S., Bollt, E., Camps-Valls, G., Coumou, D., Deyle, E., Glymour, C., Kretschmer, M., Mahecha, M. D., Muñoz-Marí, J., et al.: Inferring causation from time series in Earth system sciences, Nature communications, 10, 1–13, 2019a.

Runge, J., Nowack, P., Kretschmer, M., Flaxman, S., and Sejdinovic, D.: Detecting and quantifying causal associations in large nonlinear time series datasets, Science advances, 5, eaau4996, 2019b.

Ruprich-Robert, Y., Msadek, R., Castruccio, F., Yeager, S., Delworth, T., and Danabasoglu, G.: Assessing the climate impacts of the observed Atlantic multidecadal variability using the GFDL CM2. 1 and NCAR CESM1 global coupled models, Journal of Climate, 30, 2785–2810, 2017.

Ruprich-Robert, Y., Moreno-Chamarro, E., Levine, X., Bellucci, A., Cassou, C., Castruccio, F., Davini, P., Eade, R., Gastineau, G., Hermanson, L., et al.: Impacts of Atlantic multidecadal variability on the tropical Pacific: a multi-model study, npj climate and atmospheric science, 4, 1–11, 2021.

Saggioro, E., de Wiljes, J., Kretschmer, M., and Runge, J.: Reconstructing regime-dependent causal relationships from observational time series, Chaos: An Interdisciplinary Journal of Nonlinear Science, 30, 113 115, 2020.

Seferian, R.: CNRM-CERFACS CNRM-ESM2-1 model output prepared for CMIP6 CMIP, https://doi.org/10.22033/ESGF/CMIP6.1391, 2018.

Shiogama, H., Abe, M., and Tatebe, H.: MIROC MIROC6 model output prepared for CMIP6 ScenarioMIP, https://doi.org/10.22033/ESGF/CMIP6.898, 2019.

Si, D. and Hu, A.: Internally generated and externally forced multidecadal oceanic modes and their influence on the summer rainfall over East Asia, Journal of Climate, 30, 8299–8316, 2017.

Smirnov, D. and Bezruchko, B.: Spurious causalities due to low temporal resolution: Towards detection of bidirectional coupling from time series, EPL (Europhysics Letters), 100, 10 005, 2012.

Smith, D. M., Booth, B. B., Dunstone, N. J., Eade, R., Hermanson, L., Jones, G. S., Scaife, A. A., Sheen, K. L., and Thompson, V.: Role of volcanic and anthropogenic aerosols in the recent global surface warming slowdown, Nature Climate Change, 6, 936–940, 2016.

Stouffer, R. J., Eyring, V., Meehl, G. A., Bony, S., Senior, C., Stevens, B., and Taylor, K.: CMIP5 scientific gaps and recommendations for CMIP6, Bulletin of the American Meteorological Society, 98, 95–105, 2017.

Sutton, R. T. and Hodson, D. L.: Atlantic Ocean forcing of North American and European summer climate, science, 309, 115–118, 2005.

Swart, N. C., Cole, J. N., Kharin, V. V., Lazare, M., Scinocca, J. F., Gillett, N. P., Anstey, J., Arora, V., Christian, J. R., Jiao, Y., Lee, W. G., Majaess, F., Saenko, O. A., Seiler, C., Seinen, C., Shao, A., Solheim, L., von Salzen, K., Yang, D., Winter, B., and Sigmond, M.: CCCma CanESM5 model output prepared for CMIP6 ScenarioMIP, https://doi.org/10.22033/ESGF/CMIP6.1317, 2019.

Takahashi, C. and Watanabe, M.: Pacific trade winds accelerated by aerosol forcing over the past two decades, Nature Climate Change, 6, 768–772, 2016.

Tang, Y., Rumbold, S., Ellis, R., Kelley, D., Mulcahy, J., Sellar, A., Walton, J., and Jones, C.: MOHC UKESM1.0-LL model output prepared for CMIP6 CMIP historical, https://doi.org/10.22033/ESGF/CMIP6.6113, 2019.

Taylor, K. E., Stouffer, R. J., and Meehl, G. A.: An overview of CMIP5 and the experiment design, Bulletin of the American meteorological Society, 93, 485–498, 2012.

Trenberth, K. E. and Shea, D. J.: Atlantic hurricanes and natural variability in 2005, Geophysical research letters, 33, 2006.

Volodin, E., Mortikov, E., Gritsun, A., Lykossov, V., Galin, V., Diansky, N., Gusev, A., Kostrykin, S., Iakovlev, N., Shestakova, A., and Emelina, S.: INM INM-CM5-0 model output prepared for CMIP6 CMIP piControl, https://doi.org/10.22033/ESGF/CMIP6.5081, 2019.

Wallace, J. M. and Gutzler, D. S.: Teleconnections in the geopotential height field during the Northern Hemisphere winter, Monthly weather review, 109, 784–812, 1981.

Wang, T., Otterå, O. H., Gao, Y., and Wang, H.: The response of the North Pacific Decadal Variability to strong tropical volcanic eruptions, Climate Dynamics, 39, 2917–2936, 2012.

Watanabe, M. and Tatebe, H.: Reconciling roles of sulphate aerosol forcing and internal variability in Atlantic multidecadal climate changes, Climate Dynamics, 53, 4651–4665, 2019.

Wieners, K.-H., Giorgetta, M., Jungclaus, J., Reick, C., Esch, M., Bittner, M., Legutke, S., Schupfner, M., Wachsmann, F., Gayler, V., Haak, H., de Vrese, P., Raddatz, T., Mauritsen, T., von Storch, J.-S., Behrens, J., Brovkin, V., Claussen, M., Crueger, T., Fast, I., Fiedler, S., Hagemann, S., Hohenegger, C., Jahns, T., Kloster, S., Kinne, S., Lasslop, G., Kornblueh, L., Marotzke, J., Matei, D., Meraner, K., Mikolajewicz, U., Modali, K., Müller, W., Nabel, J., Notz, D., Peters-von Gehlen, K., Pincus, R., Pohlmann, H., Pongratz, J., Rast, S., Schmidt, H., Schnur, R., Schulzweida, U., Six, K., Stevens, B., Voigt, A., and Roeckner, E.: MPI-M MPI-ESM1.2-LR model output prepared for CMIP6 CMIP historical, https://doi.org/10.22033/ESGF/CMIP6.6595, 2019.

Wu, S., Liu, Z., Zhang, R., and Delworth, T. L.: On the observed relationship between the Pacific Decadal Oscillation and the Atlantic Multi-decadal Oscillation, Journal of oceanography, 67, 27–35, 2011.

Yan, X., Zhang, R., and Knutson, T. R.: The role of Atlantic overturning circulation in the recent decline of Atlantic major hurricane frequency, Nature Communications, 8, 1–8, 2017.

Zhang, H., Cheng, H., Spötl, C., Cai, Y., Sinha, A., Tan, L., Yi, L., Yan, H., Kathayat, G., Ning, Y., et al.: A 200-year annually laminated stalagmite record of precipitation seasonality in southeastern China and its linkages to ENSO and PDO, Scientific reports, 8, 1–10, 2018.

Zhang, R. and Delworth, T. L.: Impact of Atlantic multidecadal oscillations on India/Sahel rainfall and Atlantic hurricanes, Geophysical research letters, 33, 2006.

Zhang, R. and Delworth, T. L.: Impact of the Atlantic multidecadal oscillation on North Pacific climate variability, Geophysical Research Letters, 34, 2007.

Zhang, R., Delworth, T. L., Sutton, R., Hodson, D. L., Dixon, K. W., Held, I. M., Kushnir, Y., Marshall, J., Ming, Y., Msadek, R., et al.: Have aerosols caused the observed Atlantic multidecadal variability?, Journal of the Atmospheric Sciences, 70, 1135–1144, 2013.

Zhang, R., Sutton, R., Danabasoglu, G., Kwon, Y.-O., Marsh, R., Yeager, S. G., Amrhein, D. E., and Little, C. M.: A review of the role of the Atlantic meridional overturning circulation in Atlantic multidecadal variability and associated climate impacts, Reviews of Geophysics, 57, 316–375, 2019.

Zhang, Y., Wallace, J. M., and Battisti, D. S.: ENSO-like interdecadal variability: 1900–93, Journal of climate, 10, 1004–1020, 1997.

Ziehn, T., Chamberlain, M., Lenton, A., Law, R., Bodman, R., Dix, M., Wang, Y., Dobrohotoff, P., Srbinovsky, J., Stevens, L., Vohralik, P., Mackallah, C., Sullivan, A., O'Farrell, S., and Druken, K.: CSIRO ACCESS-ESM1.5 model output prepared for CMIP6 CMIP, https://doi.org/10.22033/ESGF/CMIP6.2288, 2019.